Alzheimer's disease ferroptotic associations with oxidative damage and neuronal loss

Max A. Thorwald[1], Jose A. Godoy-Lugo[1], Justine Silva[2], Elizabeth Head[2], Peggy A. O'Day[3], Todd E. Morgan[1], Henry Jay Forman[1,4], Caleb E. Finch[1,5]

[1]Leonard Davis School of Gerontology, University of Southern California, Los Angeles, CA.
[2]Department of Pathology and Laboratory Medicine, University of California, Irvine, CA.
[3]Life and Environmental Sciences Department, University of California, Merced, CA.
[4]School of Natural Sciences, University of California Merced, Merced, CA.
[5]Dornsife College, University of Southern California, Los Angeles, CA.

ABSTRACT: The role of reactive iron in Alzheimer's Disease (AD) remains unresolved. Little is known of how AD may alter iron transport, glutathione-mediated oxidative repair, and their associations with ApoE alleles. Postmortem brain intravascular blood was minimized by washing minced brain (n=24/group). HNE from iron-associated lipid peroxidation increased in AD prefrontal cortex by 50% for whole tissue and in subcellular lipid rafts, where Aβ-peptides are produced. HNE correlated with iron storage ferritin light chain (FTL; r=0.35); both were higher in ApoE4. Iron chelation by DFO in EFAD mice decreased HNE consistent with ferroptosis. Neuronal and synaptic loss in AD was inversely correlated to FTL (r=-0.55). AD decreased levels of ferroptosis suppressor protein 1, glutamate cysteine ligase modulator subunit (GCLM), and lipid raft glutathione peroxidase 4 (GPx4), mitigators of ferroptosis. These findings provide a mechanistic framework for iron-associated neurodegeneration during AD by impaired lipid peroxidation repair mechanisms involving glutathione.

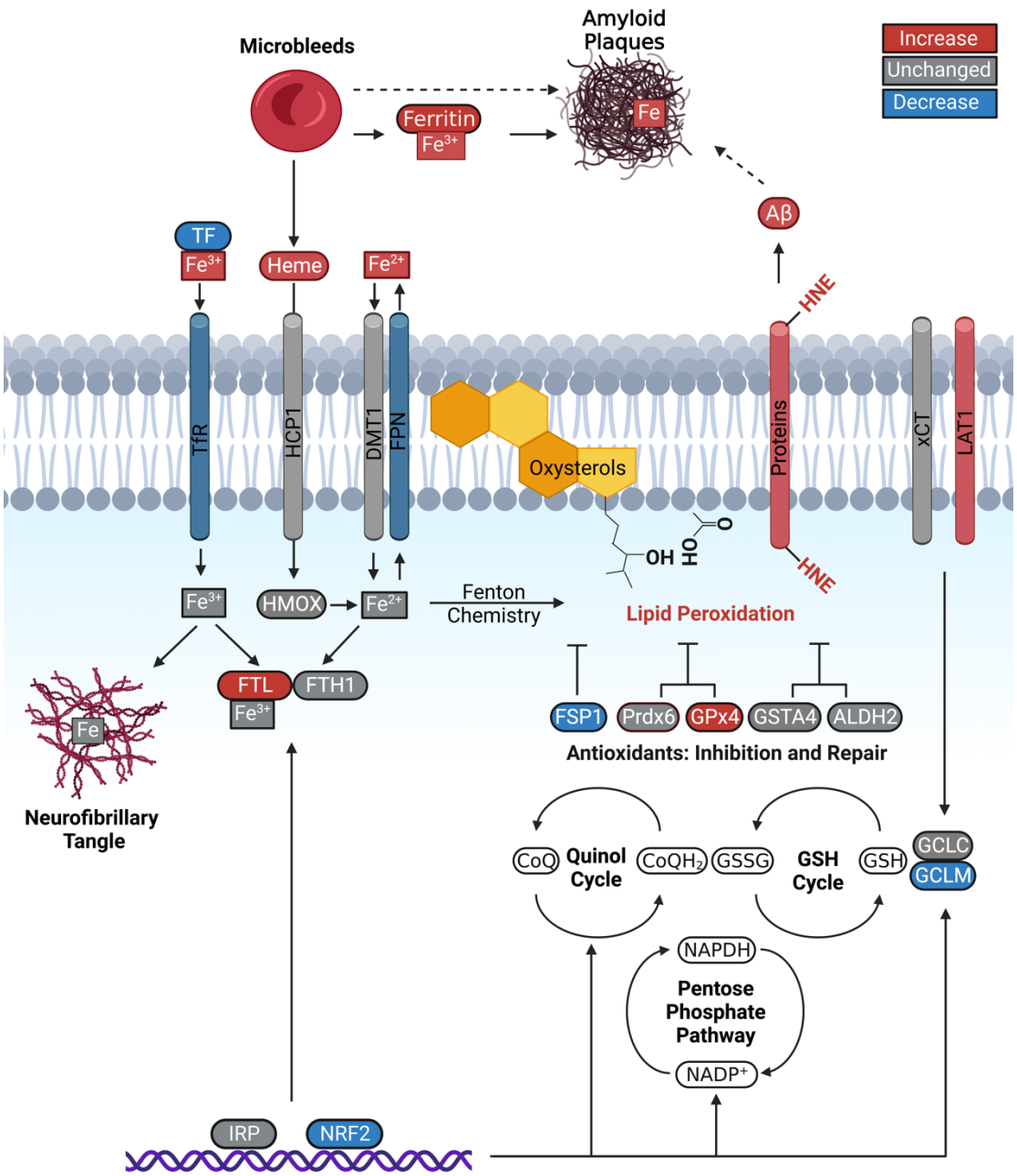

Graphical Abstract: Hypothesis: AD brain lipid peroxidation is driven by increased brain iron and decreased antioxidant defenses. Schema shows proteins that mediate iron metabolism in relation to lipid peroxidation (HNE) and antioxidant defenses in prefrontal cortex. AD-associated increase (red), decrease (blue), or no change (grey), relative to cognitively normal elderly controls. Aβ; amyloid beta, ALDH2; alcohol dehydrogenase, APP; amyloid precursor protein, DMT1; divalent metal transporter 1; FPN, ferroportin; FSP1, ferroptosis suppressor protein 1, which requires the quinol cycle to attenuate lipid peroxidation; FTH1, ferritin heavy chain; FTL; ferritin light chain; GCLC, glutathione cysteine ligase catalytic subunit; GCLM, glutathione cysteine ligase modulator; GPx4, glutathione peroxidase 4; GSH, glutathione; GSSG, glutathione disulfide; GSTA4, glutathione S-transferase A4; HMOX; heme oxygenase; IRP, iron regulatory protein; LAT1, large neutral amino acid transporter 1; LOOH, Lipid hydroperoxides; Nrf2, Nuclear factor erythroid 2-related factor 2; Prdx6, peroxiredoxin 6; TF, transferrin, TfR; Transferrin receptor; xCT, cysteine-glutamate antiporter.

INTRODUCTION:

Postmortem AD neuropathology was weakly associated with cognitive status in two large longitudinal studies[1,2]. Less than 35% of variation in terminal cognitive decline was attributable to multiple neuropathological markers including the AD traditional indicators of amyloid plaques and neurofibrillary tangles (NFT). What is missing? We hypothesize that iron-associated membrane damage contributes to pathway-specific neurodegeneration in AD.

Iron has long been linked to AD. "*The pathogenesis of Alzheimer's disease…may be a primary disturbance in the cerebral metabolism of iron"*, was proposed in 1953 by Louis Goodman from AD cases showing iron around senile plaques and neurofibrils, as detected by Prussian blue histochemistry[3]. Recent measurements by ICP-MS show association of total iron in prefrontal cortex with NFT density and rates of cognitive decline[4]. Extending the largely cancer-based ferroptosis hypothesis[5] to AD, Ayton *et al.* hypothesized that increased iron found in AD contributes to increased lipid peroxidation products. The present study examined molecular mechanisms of lipid peroxidation by iron in relation to levels of twenty proteins that mediate brain iron metabolism and the repair of lipid peroxidation.

In 1964, Hochstein hypothesized that iron oxidation caused membrane lipid peroxidation[6], followed by Ursini's 1982 discovery that the chemical reduction of phospholipid hydroperoxides by glutathione was mediated by glutathione peroxidase 4 (GPx4)[7]. The hydroxyl radical (·OH) produced from hydrogen peroxide by iron (Fenton chemistry) is widely recognized in lipid peroxidation[8].

$$\mathbf{H_2O_2 + Fe^{2+} \rightarrow {}^{\cdot}OH + OH^- + Fe^{3+}}$$

Knockout of the other seven glutathione peroxidases showed that GPx4 elimination of phospholipid hydroperoxides rather than decreased H_2O_2, is essential for preventing lethal oxidative membrane damage *in vivo*[9]. Subsequently, iron was shown to directly enhance aggregation of amyloid β-peptides[10], consistent with abundant iron in senile plaques and NFT detected by x-ray spectroscopy[10]. Specifically, plaque cores contain iron in multiple oxidation states[11]. The chemical presence of ferric iron in plaques[11,12] and in NFTs[13] confirms Goodman's initial Prussian blue histochemistry; now known to react with ferric iron[14].

Next, a specific oxidized lipid component was identified as HNE (α,β-unsaturated hydroxyalkenal 4-hydroxynonenal)[15], which is elevated in AD cerebrospinal fluid[16] and tissue[17]. HNE can form conjugates with cysteine (most reactive), histidine, and lysine[18]. In cultured neurons, iron-induced HNE and toxicity was blocked by conjugation to the antioxidant glutathione (GSH)[19]. In 2012, cancer research introduced the term ferroptosis for cell death mediated by iron-dependent lipid peroxidation. Ferroptosis was soon considered for AD and other neurodegenerative diseases[5,20,21].

Seven decades after Goodman's seminal study, brain iron levels were specifically associated with cognitive decline and AD neuropathology in the longitudinal Memory and Aging Project[4]. A mechanistic link to iron was experimentally shown for GPx4 depletion in cultured neurons exposed to hemin from degraded hemoglobin, which was blocked by iron chelation with deferoxamine (DFO)[22]. However, AD changes were inconclusive for tissue iron and for ferritin in CSF [4,23–28]. Postmortem studies in the AD brain by Ashraf et al in 2020 reported increases in prefrontal cortex of HNE and ferritin protein, and decreased ferroportin, while total brain iron did not differ in AD[24]. Conclusions were limited by the small sample of 7 brains each, AD and age-matched controls that were insufficient for analysis by sex and ApoE allele, and by the long postmortem intervals before freezing. This analysis addresses major AD unknowns for glutathione-dependent repair of lipid peroxidation[29] and the twenty proteins mediating brain iron transport and storage[5,30].

Brain cellular iron is imported by the divalent metal transporter 1 (DMT1) together with transferrin (TF) and its receptor TfR; in AD, levels of TF and TfR differ by cell type [28]. Heme iron is imported by heme carrier protein 1 (HCP1) and degraded by hemeoxygenases (HMOX1 or HMOX 2). Intracellular ferric iron is stored in complexes with ferritin light chain (FTL) after oxidation of ferrous iron (Fe^{2+}) by ferritin heavy chain (FTH1). Export of ferrous iron is mediated by ferroportin (FPN).

The tripeptide GSH mitigates the oxidation of lipids, protein amino acids, and conjugation of HNE to proteins by several enzymes (**Graphical Abstract)**. GSH is utilized to reduce hydroperoxides by the glutathione peroxidase (GPx) family and peroxiredoxin 6 (Prdx6), while the glutathione S-transferases (GST) conjugate GSH to diverse metabolites and xenobiotics. Biosynthesis of GSH depends on cystine import via the proteins xCT (SLC7A11) and LAT1 (SLC3A2/CD98). Imported cystine is then rapidly reduced to cysteine by the intracellular reducing environment[31]. The rate limiting step in GSH synthesis[32] is formation of γ-glutamylcysteine, catalyzed by glutamate cysteine ligase, with two subunits GCLC (catalytic) and GCLM (modulatory); the binding of GCLM to GCLC accelerates GSH synthesis by four-fold. Next, GSH is formed from addition of glycine to γ-glutamylcysteine by glutathione synthetase (GSS). The electrophile-activated transcription factor Nrf2 regulates gene expression of GCLC, GCLM, GPx4, and Prdx6.

To address these gaps in AD mechanism, we assayed ferritin light chain (FTL) and other iron related proteins and GSH metabolic enzymes in 24 AD and 24 age-matched control brains. Prefrontal cortex was compared with cerebellum, which has minimal AD neurodegeneration[33]. Whole tissue was compared with lipid rafts, a subcellular fraction containing the aspartyl proteases (ADAM10, BACE1, PSEN1/2) that cleave amyloid β-peptides from the amyloid precursor protein (APP). We recently reported that lipid rafts from AD brains have less APP than controls[34]; the present studies used these same brains. These relations were experimentally studied in AD transgenic mice with iron chelation by deferoxamine (DFO).

We first considered how to minimize residual erythrocytes in brain tissues that were not perfused before freezing - brain fragments are often reddish with surface blood. Residual blood will confound assays for brain iron and GSH-utilizing enzymes, because erythrocytes contain iron, ferritin, and GSH enzymes[35,36]. We introduce a washing procedure to minimize adherent and intravascular hemoglobin in unperfused brain specimens.

RESULTS:

Minimization of residual blood in postmortem brain

Cardiac perfusion of mice with heparinized saline decreased heme iron in cerebral cortex by 35% (**Table 1A**). Because perfusion is not feasible for pieces of thawed human cerebral cortex, we developed a washing procedure to minimize entrapped blood in the vasculature where prefrontal cortex was minced into 2 mm cubes, followed by gentle washing with isotonic buffer (PBS). The resulting 'washed' brain had 68% less heme than the non-perfused, a greater decrease than by perfusion.

When applied to human cortex (**Table 1B)**, washing decreased levels by 50% for heme, a-hemoglobin, and ferritin light chain. For verification and comparison with Ayton et al. 2020[4] and Ashraft et al 2021[26]: total iron in human brain was assayed by ICP-MS. Washing decreased iron by -45%, similar to the decrease by -50% in heme levels. Total iron levels for unwashed human cerebral cortex approximated those of Ayton et al. 2021[4]. Concentrations of total aluminum, copper, and zinc in human brain were not altered by washing (**Supplemental Fig. 2**), consistent with their low levels in blood. The removal of blood was further documented with α-hemoglobin and FTL, which was decreased at least 50% with washing (**Supplemental Fig. 3C-E).** Thus, entrapped intra-vascular blood may contribute 50% of the total iron in unperfused or unwashed postmortem human brain. **Table 1B** summarizes reports of 2- to 5-fold higher levels of total iron in conventional postmortem brains. While these data indicate that residual vascular blood can inflate estimates of total iron and extravascular heme, some vascular blood must remain. Postmortem perfusion should be feasible before brain removal in future studies.

Table 1 Heme and Iron content of prefrontal cortex

A. Mouse, wildtype

	Non-perfused	Perfused PBS	Perfused PBS + Heparin	Non-Perfused + Washed
Heme/mg wet brain	3.1 ± 0.2	2.1 ± 0.2* (-32%)	2.0 ± 2.3** (-35%)	1.3 ± 0.2*** (-68%)

B. Human

Source	Unwashed	Washed
Total iron, ug/g wet brain	45 ± 4.9	26 ± 1.4 ****, -45%
Ayton et al. 2021[4]	~55	N/A
Ashraf et al. 2020[24]	~290	N/A
Heme/mg	7.1 ± 0.4	3.6 ± 0.2, ****, -50%
a-Hemoglobin, ug/mg	1,644 ± 131	815 ± 61, ****, -50%
Ferritin light chain (RFUs)	100 ± 9	235 ± 17, **** -60%

C. Sources of Iron and Ferritin

Compartment	Total iron	Ferritin
Brain, unwashed	50 ug/g wet brain	0.135 ug/g
Blood	3,500 ug/mL	3.8-14 ug/mL
Serum	1.3 ± 0.14 ug/mL	0.011-3.4 ug/mL
CSF	0.061 ± 0.006 ug/mL	0.012 ug/mL

Table 1: Heme and total iron in prefrontal cortex were assayed for effects of washing to minimize residual intravascular blood. **A**) mouse (C57BL/6J, 6 mo; n=5-6); **B**) human (AD; n=24) and controls (65+ yr; n=24) prefrontal cortex (Brodmann regions 8-10); **C)** Iron[4,37,38] and ferritin[23,38,39] in brain, blood, serum, and CSF. The ferritin complex in erythrocytes and tissue include FTL and FTH1. Isotonic phosphate buffered saline (PBS; pH 7.4) was used for aortic perfusion of mouse and for washing of minced mouse and human brain. Prefrontal cortex 30 mg was minced into 2 mm cubes and 'washed' by gentle vortexing in PBS. Heme and α-hemoglobin per mg tissue were assayed spectrophometrically relative to unwashed brain (**Supplemental Fig. 3**). For total iron measurement by ICP-MS, brain cubes were gently sheared in PBS by polyethylene pestle (PES-15-B-SI, Axygen). Total iron levels from Ashraf[41] was estimated as Fe/g protein, assuming 1 g protein/12 g wet weight brain. Brain iron and ferritin by compartment for human are >95% below blood levels, assuming 1 ml volume is equivalent to 1 gram wet brain. Significance by one way ANOVA (mouse) with Tukey's posthoc, or 2-tailed t-test (human): *p<0.05, **p<0.01, ***p<0.001, ****p<0.0001.

Lipid peroxidation and heme are increased in AD

Washed brain samples were assayed for oxidative damage by measuring two protein adducts, HNE and 3-nitrotyrosine (NT) (**Fig. 1**). For the following data, cognitive status was defined by clinical criteria for AD and age-matched controls; further studies (**Fig. 7, Supplemental Table 1**) include postmortem Braak scores for NFT[42].

Prefrontal cortex AD total iron did not differ (**Fig. 1B**), while heme increased +25% (**Fig. 1C**). AD had 50% more HNE and NT than controls (**Fig. 1D,E**). HNE correlated with heme (r=0.32, p=0.025), unlike NT (r=0.11, p=0.47; not shown). The absence of heme-NT correlation suggests a different pathway than for heme-iron production of HNE. For example, aggregated human Aβ42 stimulates production of neurotoxic peroxynitrite, shown by us *in vitro*[43].

Cerebellum (**Extended Figs.**) was compared with prefrontal cortex as an adjacent brain region with less AD neurodegeneration[33]. AD cerebellar heme was 40% higher, paralleling cortex (**Ext. Fig. 1C**). Cerebellum HNE increased 30% in AD (**Ext. Fig. 1E**), while NT did not differ (**Ext. Fig. 1D**).

ApoE alleles and sex influenced HNE levels, but not NT. The ApoE4 prefrontal cortex had 35% more HNE than ApoE3 (**Fig. 1F**); cerebellar HNE did not differ by ApoE allele (**Ext. Fig. 1F**). Sex differences did not parallel apoE alleles. For female AD, prefrontal cortex had 60% more HNE than cognitively normal, whereas males did not differ in HNE by cognitive status (**Fig. 1G**). Sex-ApoE interactions were not statistically evaluated because of the small sample size; data are shown in **Supplemental Tables 1 and 3**.

To experimentally evaluate these findings, EFAD mice were given iron chelation by DFO in diet for two weeks or by intraperitoneal injection (IP) twice daily for one week. Data are shown for both dietary DFO and IP (see Extended figures for separate treatments). DFO treatment decreased HNE adducts by 35%, while NT levels were unchanged (**Fig. 1H,I**).

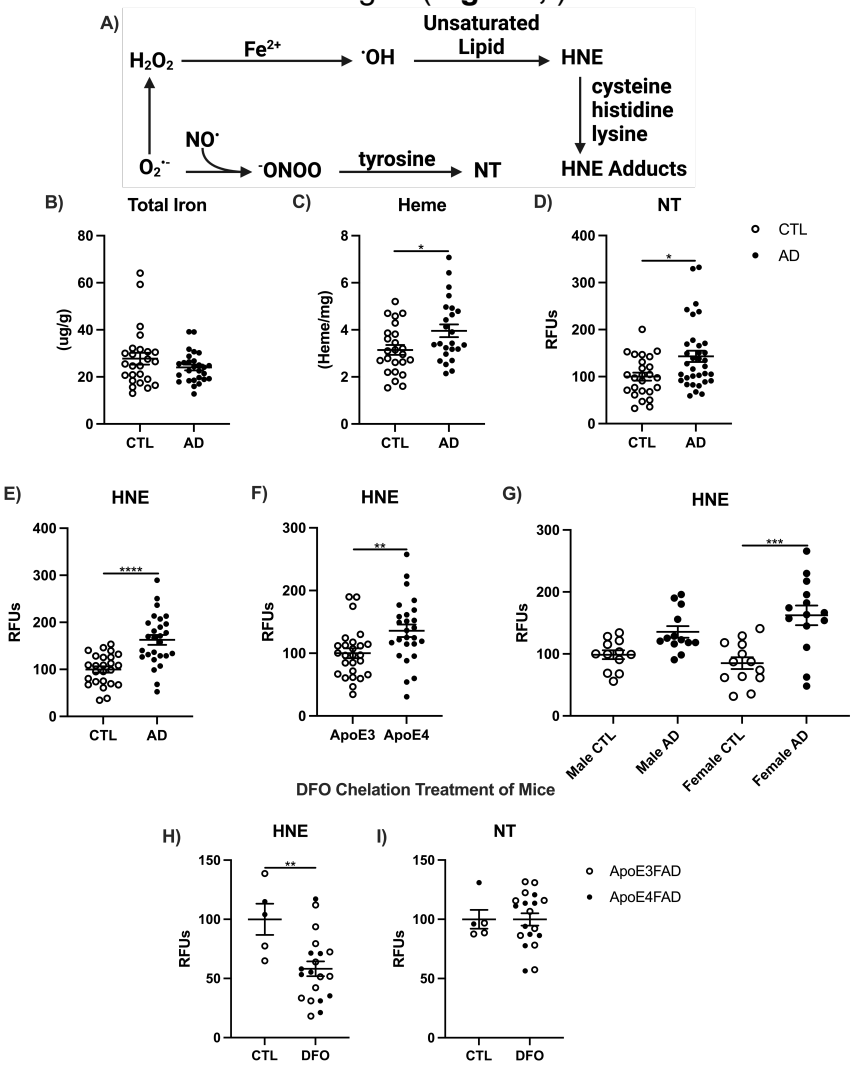

Figure 1: Oxidative damage to prefrontal cortex proteins (HNE, NT) in age matched AD (n=27) and cognitively normal control (CTL; n=25). **A)** Schematic representing oxidative damage to lipids and proteins. Hydroxyl radicals (·OH) are produced during oxidation of Fe^{2+} or Cu^{2+} ('Fenton chemistry') and may oxidize adjacent proteins, lipids or nucleic acids. HNE can alter proteins via Michael addition products through its double-bonded carbons, or by forming Schiff bases through its aldehyde moiety. The bottom line reaction shows the iron-independent oxidative pathway to form peroxynitrite $^{-}$ONOO from $O_2^{\bullet-}$ and ·NO, which can then oxidize tyrosine to NT. Aggregated human Aβ42 stimulated formation of peroxynitrite which was

neurotoxic in vitro[43]. Non-heme iron also mediates lipoxygenase activity[44]. Prefrontal cortex from Brodmann area 8, 9, or 10 and cerebellum was washed measurements for **B)** Total iron, measured by ICP-MS **(Table 1B)**, **C)** heme, and dot blots for **D)** NT, and HNE presented as **E)** cognitively normal vs AD, **F)** ApoE allele, or **G)** sex as relative fluorescent units (RFUs). DFO chelation treatment of ApoEFAD mice, dot blots for **H)** HNE, and **M)** NT. Significance by 2-tailed t-test (B-F, H-I) or one-way ANOVA (G): *p<0.05, **p<0.01, ***p<0.001, ****p<0.0001.

Next, we analyzed AD associations with oxidative damage and heme iron in specific pathways that mediate brain iron transport and storage. GSH is the main oxidative repair mechanism, biochemically reduced by the NADPH produced by the pentose phosphate pathway (**Graphical abstract**). Iron deposits and membrane oxidative repair were analyzed for levels of twenty proteins that had statistically significant AD changes.

Iron protein metabolism is decreased in AD

Iron transport proteins were decreased in AD (**Fig. 2A-E**): transferrin and its receptor TfR (-25%); iron export protein FPN (-30%), with a trend for DMT1 (-30%; p=0.13). Correspondingly, AD increased ferritin light chain (FTL) (+75%) (**Fig. 2H**), while ferritin heavy chain (FTH1) was not changed by AD (**Fig. 2I**). The increased FTL in AD confirms Ashraf [24] who also reported increased FTH1, not found in our larger sample. Increased brain FTL is consistent with reports in studies of cerebrospinal fluid, microglia, and neuritic plaques during AD[23,25,27], which could arise from multiple cellular sites (**Table 1C**). Relationships for iron import/export included negative correlations between iron storage protein FTL with iron import by TfR (r=-0.30, p=0.04) and export by FPN (r=-0.36, p=0.01; **Fig. 2J**). ApoE4,4 had 2-fold higher FTL than ApoE3,3 and ApoE3,4 in prefrontal cortex.

The cerebellum differed from prefrontal cortex in the absence of higher FTL in AD (**Ext. Fig. 2H**) or ApoE4 carriers **(Supplemental Table 3)**. AD cerebellum had higher transferrin (TF), while TfR and DMT1 were decreased, paralleling the AD cortex (**Ext. Fig. 2A-C**). HMOX1 decreased 40% in AD cerebellum, while HMOX2 was unchanged **(Ext. Fig. 2F-G**). These brain region differences in oxidative damage are consistent with the relative resistance of cerebellum to AD damage.

Mice treated with DFO chelation had increased iron import proteins TF (+45%) and TfR (+70%) but not DMT1 (**Fig. 2K-M**). Iron export protein FPN decreased 30% with DFO treatment (**Fig. 2N**). Heme catabolism proteins HMOX1 and HCP1 were unchanged with DFO (**Fig. 2O,P**). Iron storage proteins FTL (+40%), FTH1 (+70%) after DFO treatment in ApoEFAD mouse cortex (**Fig. 2Q,R**).

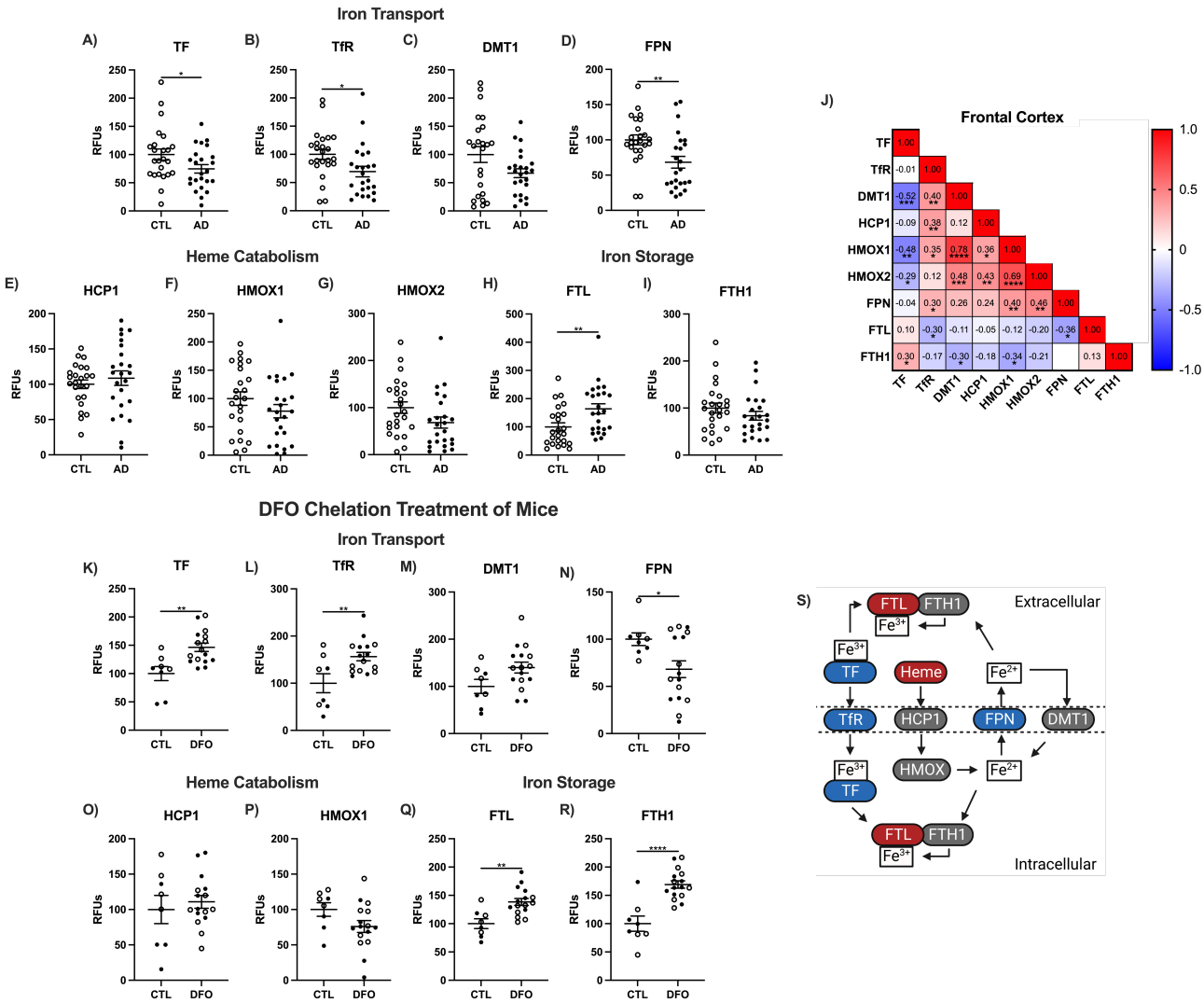

Figure 2: Iron transport and metabolism in AD prefrontal cortex (n=24) compared to cognitively normal (n=24). Relative fluorescent units (RFUs) from Western blots. **A)** transferrin (TF), **B)** transferrin receptor (TfR/CD71), **C**) divalent metal transporter 1 (DMT1), **D)** ferroportin (FPN), **E)** heme carrier protein 1 (HCP1), **F)** hemeoxygenase 1 (HMOX1), **G)** heme oxygenase 2 (HMOX2), **H)** ferritin light chain (FTL), **I)** ferritin heavy chain 1 (FTH1), **J)** Correlation matrix for iron metabolism in clinical AD. Western blots of DFO treated ApoEFAD mouse cortex for **K)** TF, **L)** TfR, **M)** DMT1, **N)** FPN, **O)** HCP1, **P)** HMOX1, **Q)** FTL, and **R)** FTH1. **S)** Schema of AD changes: blue, decrease; red, increase. Significance, 2-tailed t-test (A-I, K-R) or Spearman correlation (J): *p<0.05, **p<0.01, ***p<0.001, ****p<0.0001.

GSH synthesis is decreased with AD

GSH enzymes showed AD selective changes in relation to iron transport proteins in whole brain tissue, and in subcellular lipid rafts wherein neurons generate amyloid β-peptides from the amyloid precursor protein (APP)[34]. Lipid antioxidant mechanisms independent of GSH include ferroptosis suppressor 1 (FSP1), which utilizes $CoQH_2$ to reduce lipid hydroperoxides through the quinol cycle. In cortex, GPx4 protein level was doubled in AD relative to controls, while FSP1 was decreased 40% (**Fig. 3A,D**). FSP1 was decreased in AD cerebellum; additional data in **Ext Fig. 3**.

Because GSH has a critical role in prevention of lipid peroxidation, we examined enzymes of the GSH synthesis cycle (**Graphical Abstract)**. In AD prefrontal cortex, the glutamate-cysteine ligase subunits were differentially altered for AD: only the modulatory subunit GCLM was decreased by -

60%; the catalytic subunit GCLC was unaltered (**Fig. 3H,I**). LAT1 (L-type amino acid importer transporter) increased 33% in AD, while xCT did not differ, contrary to the 20% increase observed by Ashraf *et al.* 2020[24] (**Fig. 3J,K**). Two enzymes of GSH synthesis were not altered in AD cortex: glutathione synthase (GSS), the final step in GSH synthesis (**Fig. 3L**) and glutathione reductase (GSR) (**Fig. 3M**), which utilizes NADPH to reduce glutathione disulfide back to GSH. Cerebellum GCLM protein decreased by 35%, consistent with cortex (**Extended Fig. 3H**).

Related metabolic cycles also showed selective AD changes. For the pentose phosphate pathway, glucose 6-phosphate dehydrogenase (G6PD) was decreased by 45% in AD cases relative to controls, while phosphogluconate dehydrogenase (PGD) was unchanged (**Fig. 3N,O**). These enzymes oxidize glucose to generate NAPDH required by GSR for reduction of GSSG. The NADPH-producing enzymes G6PD and PGD were positively correlated with GSR (both $r=0.31$, $p=0.03$). The amino acid importer LAT1 and cystine importer xCT were positively correlated ($r=0.49$, $p<0.001$; **Fig. 3P**). Cerebellum GSR was also positively correlated with G6PD ($r=0.42$, $p=0.003$; **Ext. Fig. 3P2**).

DFO chelation treatment of mice increased GPx4 (+80%) and GPx1 (+70%) (**Fig. 3Q,R**). HNE clearance protein GSTA4 increased 45% with iron chelation (**Fig. 3U**). GSH biosynthesis proteins GCLC (+50%) and xCT (+60%) also increased with DFO treatment (**Fig. 3X,Y**).

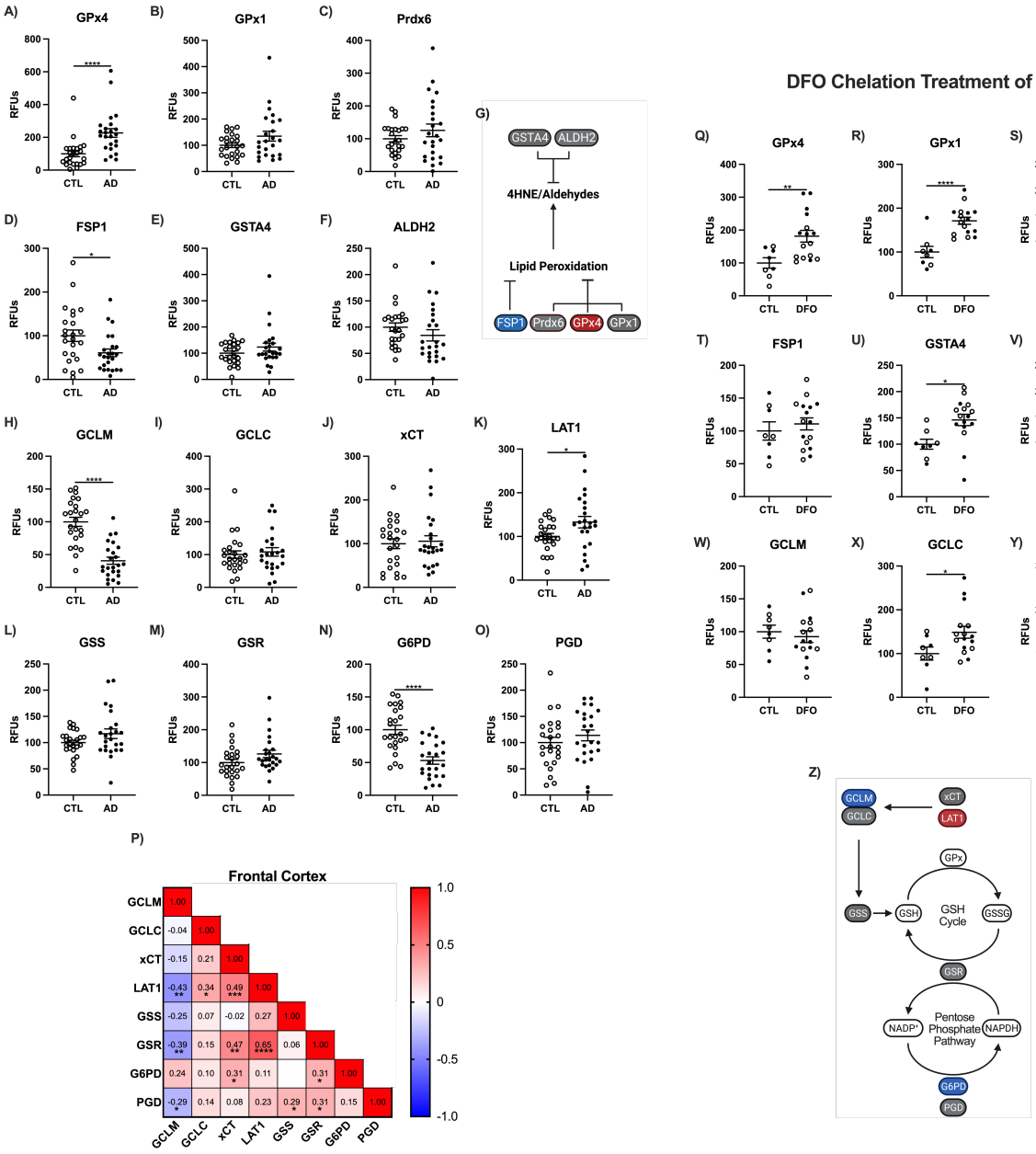

Figure 3: Enzymes that repair or mitigate lipid peroxidation and facilitate GSH production. Western blots shown as relative fluorescent units (RFUs) for frontal cortex from whole tissue lysate for antioxidants **A)** GPx4, **B)** GPx1, **C)** Prdx6, **D)** FSP1, **E)** GSTA4, and **F)** ALDH2. **G)** Enzymatic repair of lipid peroxidation. GSH cycle enzyme levels by Western blots, as relative fluorescent units (RFU). **H)** GCLM, **I)** GCLC, **J)** xCT/SLC7A11, **K)** LAT1, **L)** GSS, **M)** GSR, **N)** G6PD, and **O)** PGD. **P)** Correlation matrix for GSH cycle enzymes. Western blots of DFO treated ApoEFAD mouse cortex for **Q)** GPx4, **R)** GPx1, **S)** Prdx6, **T)** FSP1, **U)** GSTA4, **V)** ALDH2, **W)** GCLM, **X)** GCLC, and **Y)** xCT/SLC7A11. **Z)** Schema of GSH metabolic enzymes and pentose phosphate pathway. AD (n=24) increase (red), decrease (blue), no change (grey), relative to cognitively normal controls (n=24); not measured (white). Significance by 2-tailed t-test (A-H, Q-I) or Spearman correlation (I): *p<0.05, **p<0.01, ***p<0.001, ****p<0.0001.

Iron transcription factors did not differ by AD

Transcription factors were examined for DNA binding proteins that are directly influenced by intracellular iron (IRP1/2, NCOA4), or indirectly (Nrf2) (**Ext. Fig. 8A**). IRP1 and IRP2, did not differ in AD cases compared to controls in cortex (**Ext. Fig. 8B,C**). However, nuclear receptor coactivator A4 (NCOA4; lysosomal degradation of ferritin) was 30% higher in AD (**Ext. Fig. 8F**).

Transcription factors Nrf2 and NF-kB that regulate multiple genes of detoxification and inflammation were differentially altered: Nrf2 was -75% lower in AD, while NF-κB p65 transcription factor subunit was 2-fold higher (**Ext. Fig. 8D,E**). Other transcription factors were unchanged by AD (**Ext. Fig. 8**).

DFO chelation treatment of mice decreased total IRP2 55% but not IRP1 (**Ext. Fig. 8G,H**). Paralleling the antioxidant and iron protein increases, total Nrf2 protein increased 1.5-fold with DFO diet and 4-fold in I.P. animals. DFO IP had total Nrf2 levels 60% higher than DFO in diet (**Ext. Fig. 8I**). Total NCOA4 was unaltered with DFO (**Ext. Fig. 8J**).

Lipid peroxidation is increased and antioxidant defense is diminished in AD lipid rafts

Subcellular lipid rafts (LR) were examined in these same samples for oxidative changes relevant to amyloid β-peptide production from APP (**Fig. 4**). Before evaluating AD, we defined which GPx isoforms are present in lipid rafts. As expected, GPx4 was present, as well as GPx1 (**Supplemental Fig. 4**). Prdx6, another GSH utilizing lipid hydroperoxide reducing enzyme, was absent in lipid rafts (not shown), despite its presence in whole tissue cortex (**Fig. 3D**).

AD cortex had increased lipid raft oxidation: HNE, +165%; NT, +65% (**Fig. 4G,H**), paralleling increases observed in total tissue (**Fig 1C,D)**. Similarly, lipid raft HNE had a smaller AD increase in cerebellum (+45%) than cortex (+160%; **Ext. Fig. 4H**). LR HNE levels increased in carriers with at least ApoE4 allele in prefrontal cortex by 80% (**Fig. 4I**) and 30% in cerebellum (**Ext. Fig. 4I**). Sex did not influence HNE levels by AD in prefrontal cortex, however females had higher baseline HNE in cognitively normal for cerebellum (**Ext. Fig. 4K**).

AD decreased the membrane protective enzymes GPx4 (30%), GPx1 (50%), and ALDH2 (40%; **Fig. 4B-D**), consistent with membrane damage in AD. Aβ clearance proteins ApoE and LRP1 decreased in AD rafts by 40% in prefrontal cortex (**Fig. 4E,F**) with similar results in cerebellum (**Ext. Fig. 4E,F**). The Discussion considers how these changes may influence the production of amyloid β-peptides.

Non-raft membrane fraction (NRM) showed increased oxidative damage only for NT (+35%) but not HNE (**Ext**. **Fig. 4L**). AD vs CTL did not differ for HNE or by ApoE allele (**Ext. Fig. 4N,O**). NRM GPx4 levels were not altered by AD (**Fig 4N**). GPx4's in the LR was 2-fold higher than the NRM from the same tissues (**Ext. Fig. 4Q**).

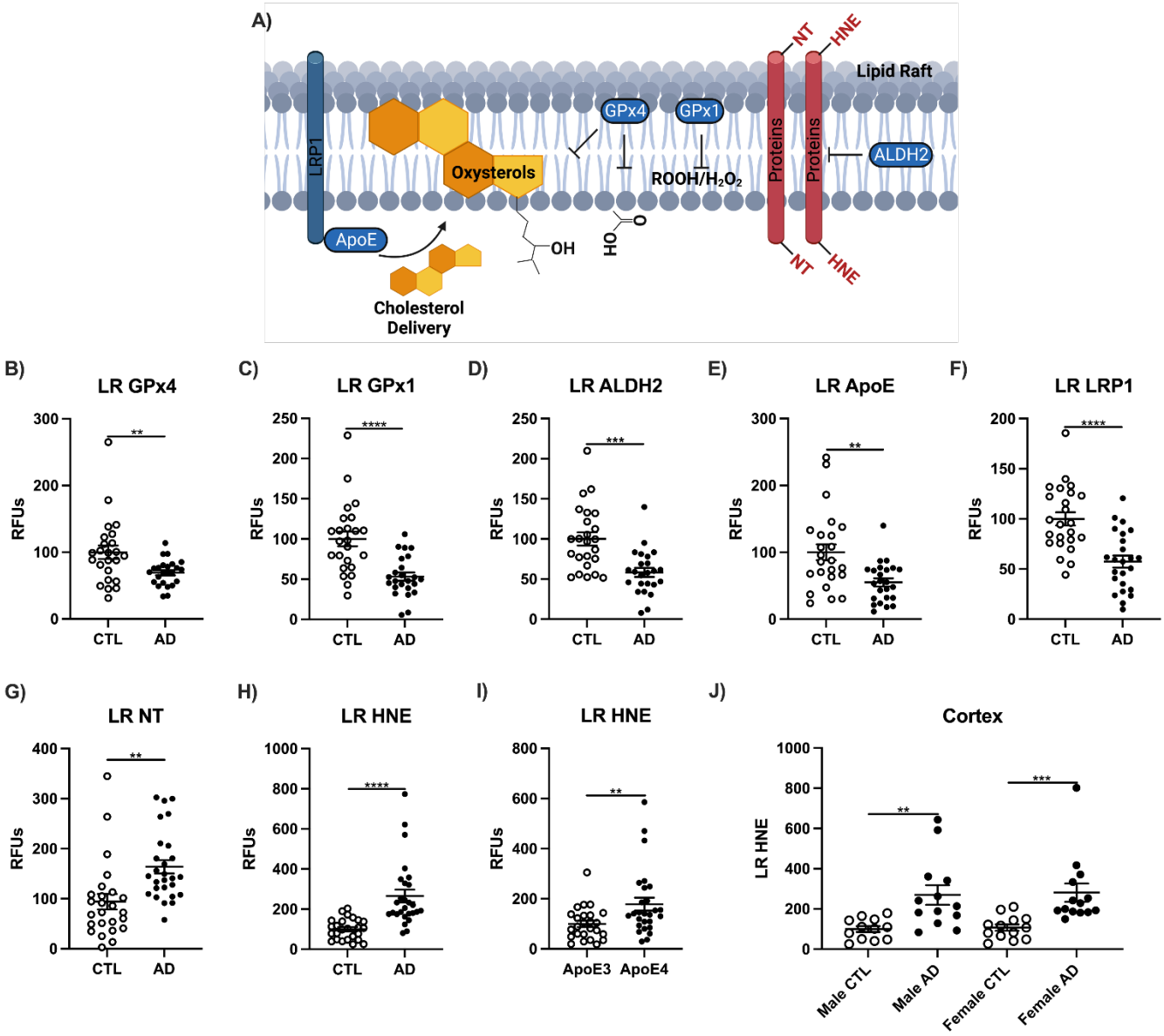

Figure 4: A) Schema of lipid raft damage, protective mechanisms, and cholesterol shuttling in AD prefrontal cortex. Western blots (n=24/group) as relative fluorescent units (RFUs) of lipid raft **B)** GPx4, **C)** GPx1, **D)** ALDH2, **E)** ApoE, **F)** LRP1. Dot blots (n=25-27/group) for **G)** NT, and HNE presented as **H)** CTL vs AD, **I)** ApoE allele, and **J)** sex. B-I) Significance by 2-tailed t-test or J) one-way ANOVA with Tukey's posthoc: *p<0.01, **p<0.01, ***p<0.001, ****p<0.0001.

Ferroptosis markers in AD

Proteins and oxidative modifications involved in ferroptosis differed by clinical AD status in whole tissue prefrontal cortex and lipid rafts (**Fig. 5A**). Both whole tissues and rafts showed AD increases of iron storage and reduced iron export (**Fig. 5B,C**); increased lipid peroxidation particularly in membranes (**Fig. 5D,E**); increased ferritin degradation (ferritinophagy) (**Fig. 5F**), lower Nrf2 (**Fig. 5G**) and its target antioxidant genes that mitigate lipid peroxidation (**Fig. 5H-M**). Cerebellum had fewer AD alterations of ferroptosis-related proteins (5/10) than cortex (**Ext. Fig. 5**). Notable changes in cerebellum are decreased GCLM (-35%), lipid raft GPx4 (-40%), and FSP1 (-40%) that paralleling cortex (**Ext. Fig 5I,L,M**).

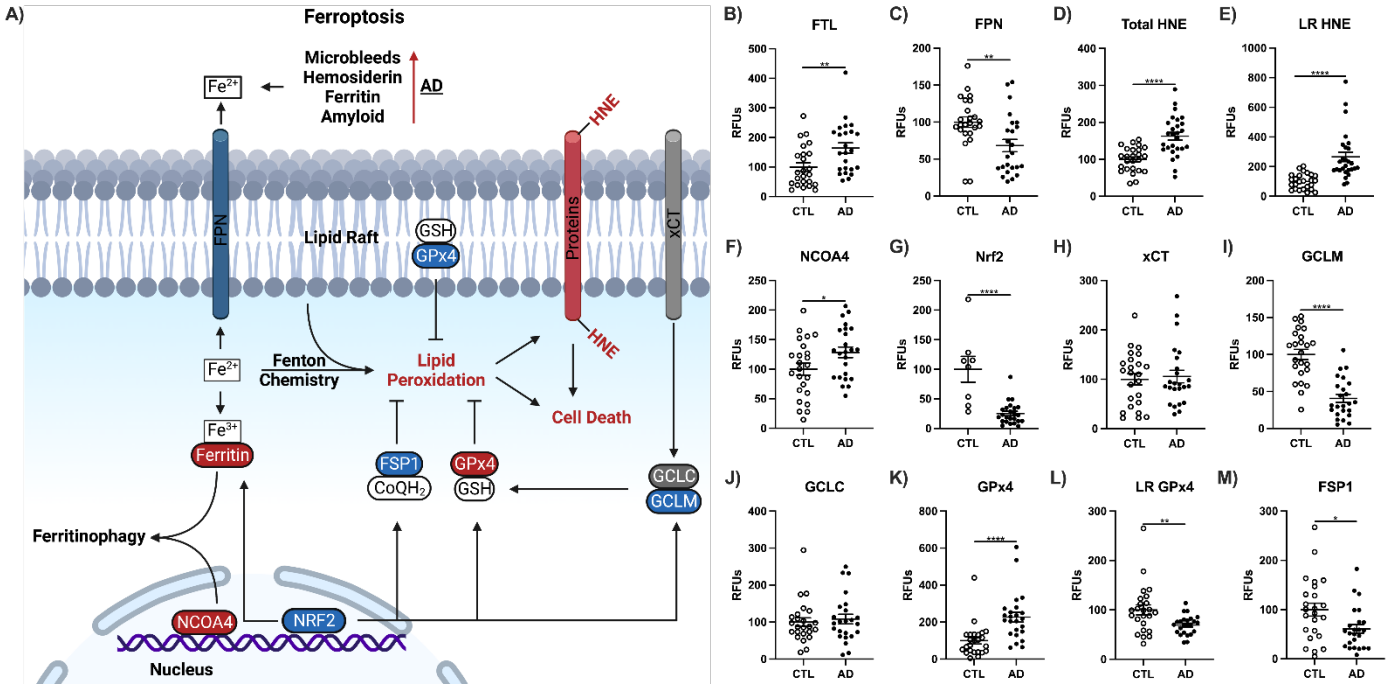

Figure 5: Ferroptosis schema with consolidated data from prior figures. **A)** Schema of ferroptosis markers related to iron transport, lipid rafts, and oxidative damage mitigation. **B)** FTL, **C)** FPN, **D)** HNE, **E)** lipid raft HNE, **F)** NCOA4, **G)** Nrf2, **H)**, xCT, **I)**, GCLM, **J)** GCLC, **K)** GPx4, **J)** Lipid raft GPx4, and **M)** FSP1. Significance by 2-tailed t-test: *p<0.05, **p<0.01, ****p<0.0001.

Neuronal loss in AD is associated with increased ferritin, lipid peroxidation, and diminished antioxidant defense

While neuronal loss dramatically increases in AD, the relation of neuronal loss is undefined for iron stores and membrane damage in relation to clinical AD and Braak stage. Neurons and synapses of prefrontal cortex were analyzed for organelle-specific proteins of NeuN (neuronal nuclear antigen), presynaptic SYP (synaptophysin1), and postsynaptic PSD95 (postsynaptic density protein 95). Statistical significance was analyzed in two ways: as above, by comparing pre-mortem clinical status of dementia versus controls; additionally, we examined neuron loss markers in relation to postmortem Braak scores 0-6 for density and distribution of NFTs. By both clinical and Braak measures, AD cortex had the expected major loss of neuron cell bodies (NeuN, -50%) and synapses (PSD95, -40%; **Fig. 6A,C**). Neuronal markers varied inversely with cortex tissue levels of heme by Braak score (**Fig. 6D**), while NeuN varied inversely with ferritin light chain, FTL (r=-0.56, p<0.0001). The relationship for NeuN and heme was significant for Braak stage (r=-0.29, p=0.04) but not for clinical status. These inverse associations are the first direct associations of brain iron markers with brain region-specific neuron loss during AD. The inverse variation of NeuN with HNE (r =-0.46, p<0.001) strengthens the relationship of lipid peroxidation to neuron loss. Many of these relationships were weakened or absent from cerebellum, consistent with its reduced neuronal loss (**Ext. Fig. 6**).

Because cognitive status had shown limited correlation for postmortem AD-related indices in two large longitudinal studies[1,2], we examined the present data for disjunction and overlap by both premortem clinical AD and by postmortem Braak. The Venn diagram for neuronal markers shows 41% overlap of AD vs controls by clinical status and Braak score (**Fig. 6E**) for all metrics in **Fig. 6D**. The positive correlation between NeuN and FPN protein levels was the only relationship shared by both criteria and in cortex and cerebellum: (**Ext. Fig. 6D-F**). This singularity suggests the importance of iron export by FPN for neuronal survival.

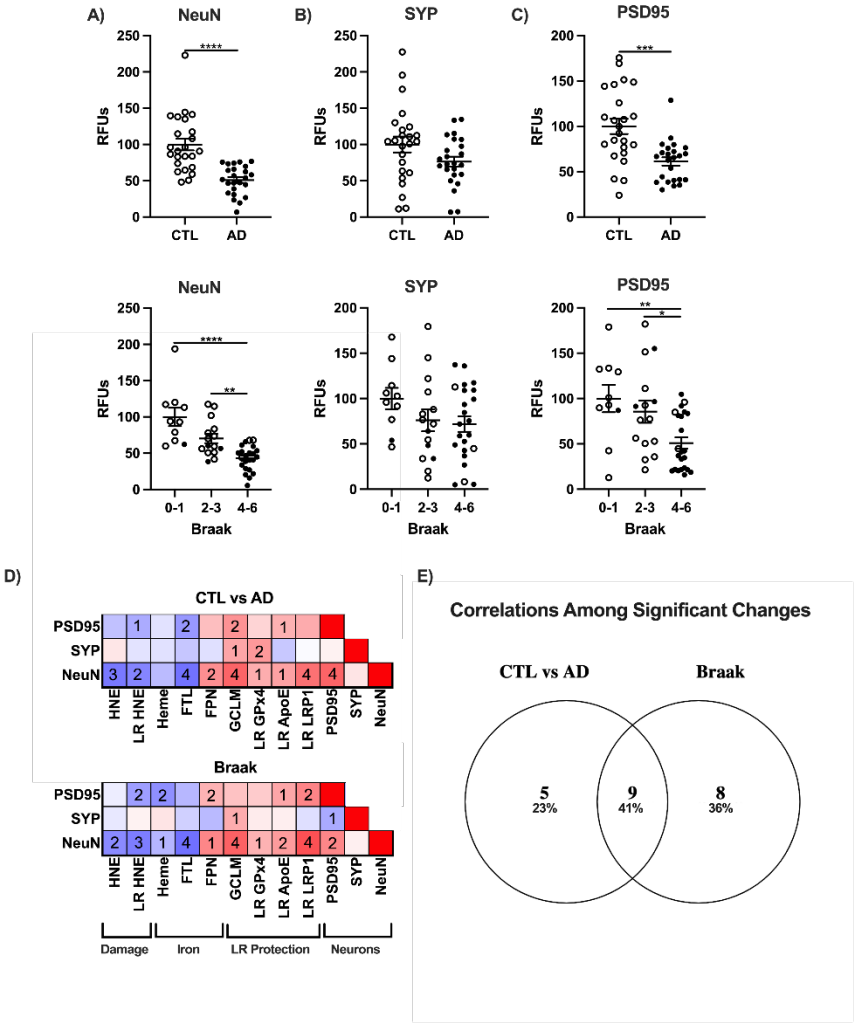

Figure 6: Neuronal loss in AD prefrontal cortex. Western blots as relative fluorescent units (RFU) of neuronal markers presented as CTL vs AD or Braak stage[34]. **A)** neuronal nuclei antigen (NeuN), **B)** synaptophysin 1 (SYP), **C)** postsynaptic density protein 95 (PSD95). **D)** Correlation matrix for variables with significant relationships to NeuN and **E)** Venn diagram comparison. Significance by 2-tailed t-test (CTL vs AD), one way ANOVA (Braak) with Tukey's posthoc, or by Spearman correlation: *p<0.05, **p<0.01, ***p<0.001, ****p<0.0001. Correlation matrix: 1, p<0.05; 2, p<0.01; 3, p<0.001; 4, p<0.0001.

ApoE allele associations with lipid rafts, lipid peroxidation, and antioxidant defense

NeuN was 50% lower in ApoE4,4 carriers than E3,3 and 3,4 (**Fig. 7A**). LR total cholesterol (-25%) and protein (-50%) had the largest deficits in ApoE4,4 carriers (**Fig. 7C,D**). Total Aβ fibrils were higher by 140% in ApoE4,4 carriers than E3,3 (**Fig. 7F**). The amyloid clearance proteins ApoE and LRP1 were 50% lower in ApoE4,4 (**Fig. 7G,H**). Iron storage protein FTL (+110%) was highest in ApoE4,4 carriers with matched increases in LR HNE (+185%) adducts (**Fig. 7I,J**). Antioxidant GPx4 (-50%) and GSH cycle enzyme GCLM (-60%) were both decreased in ApoE4,4 cortex (**Fig. 7K,L**). All LR markers were negatively correlated with Aβ fibrils (**Fig. 7M**). Aβ fibrils also correlated with LR HNE levels (r=0.56, p<0.0001).

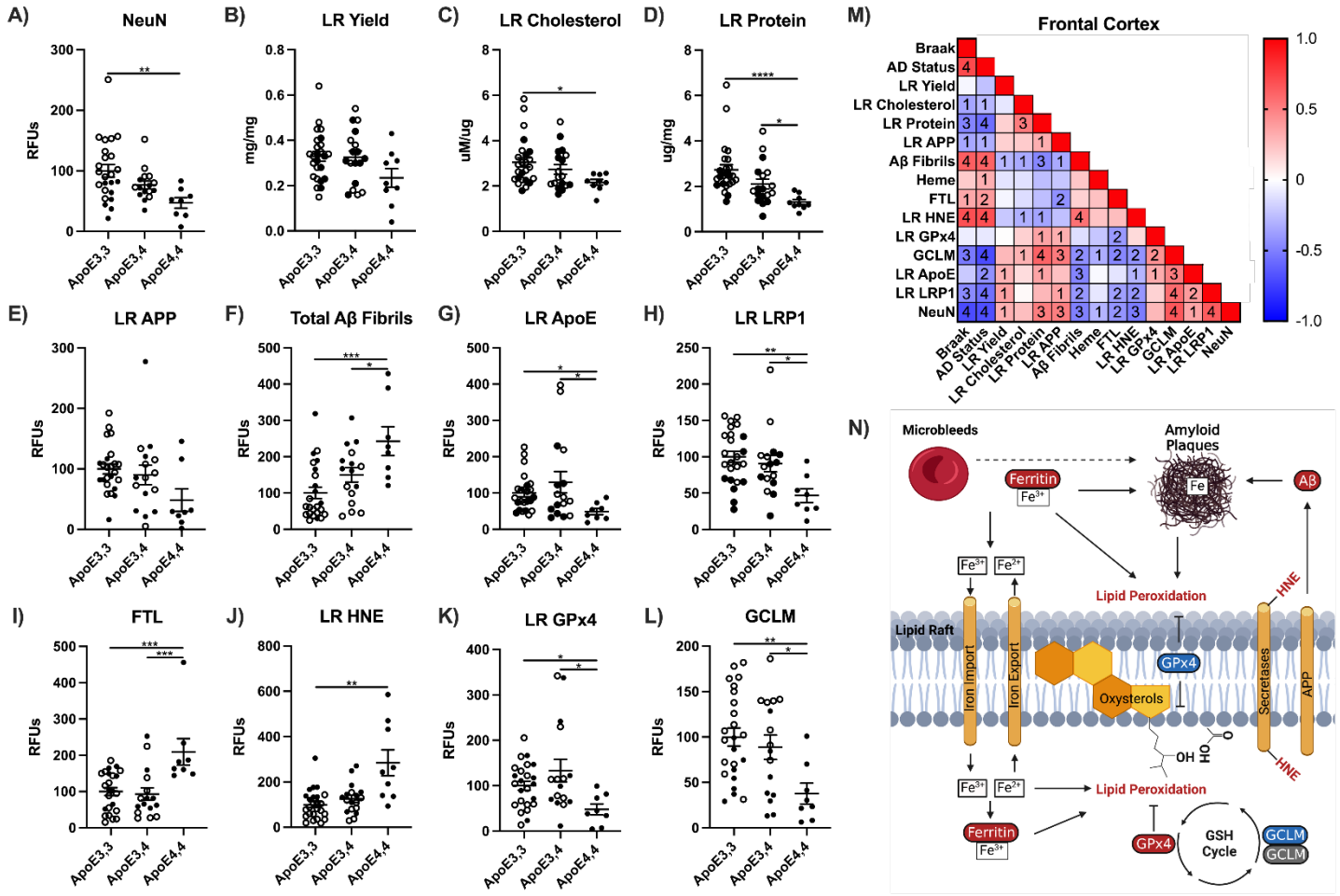

Figure 7: ApoE allele differences are associated with lipid rafts, antioxidant defense, and amyloid. Levels of **A)** NeuN, **B)** LR yield, **C)** LR cholesterol, **D)** total LR protein, **E)** LR APP, **F)** total Aβ fibrils, **G)** LR ApoE, **H)** LR LRP1, **I)** FTL, **J)** LR HNE, **K)** LR GPx4, and **L)** GCLM in prefrontal cortex of cognitively normal and AD. **M)** Correlation matrix of proteins analyzed by ApoE allele. **N)** Hypothesis linking oxidized lipid rafts to amyloid processing. One way ANOVA with Tukey's posthoc, or by Spearman correlation: *p<0.05, **p<0.01, ***p<0.001, ****p<0.0001. Correlation matrix: 1, p<0.05; 2, p<0.01; 3, p<0.001; 4, p<0.0001.

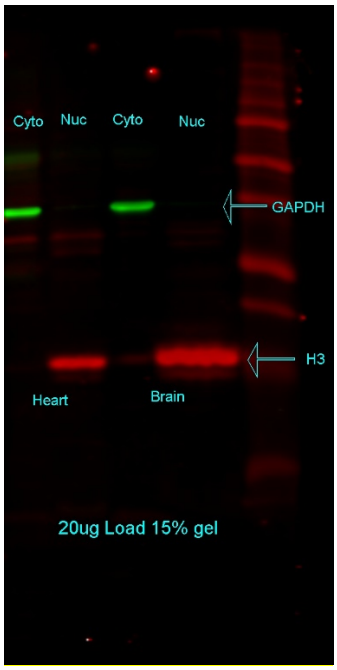

Supplemental Figure 1: Nuclear and cytosolic fractions from mouse heart and cortex. Lysates probed by Western blot for histone 3 (H3, nuclear marker) and glyceraldehyde 3-phosphate dehydrogenase (GAPDH, cytosolic marker).

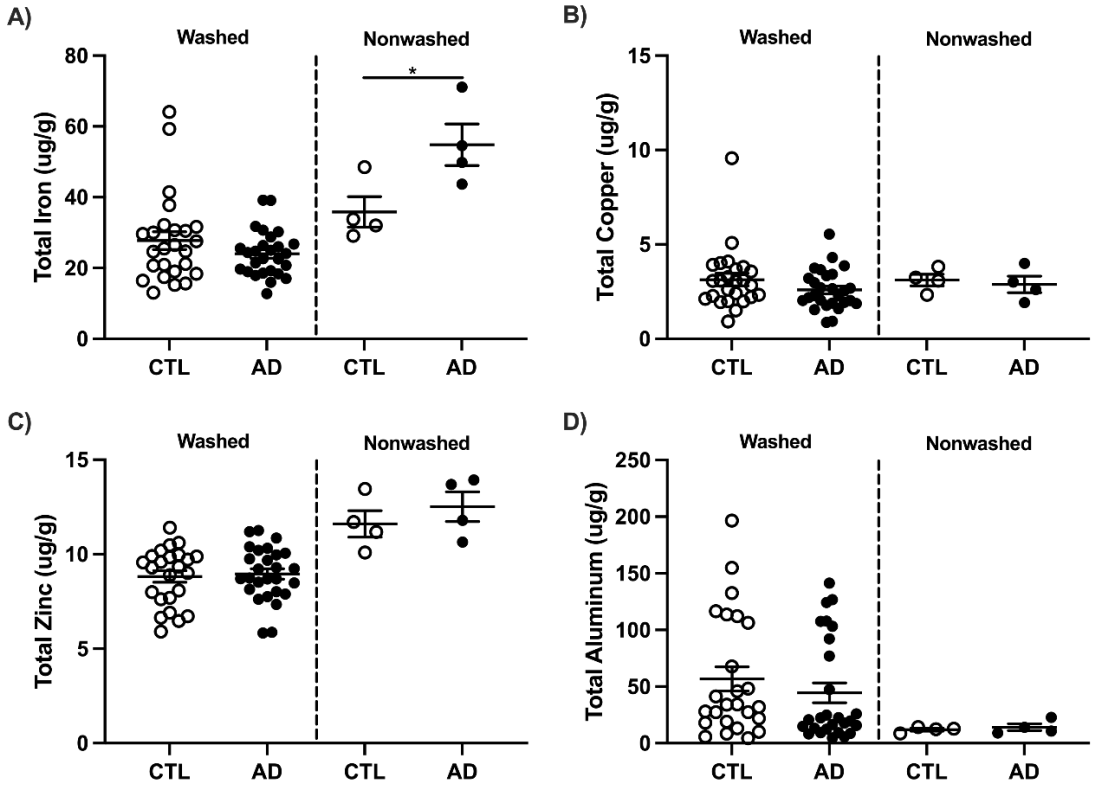

Supplemental Figure 2: Total **A)** Iron, **B)** Copper, **C)** Zinc, and **D)** Aluminum concentrations measured by ICP-MS (Table 1). **A-D,** Human prefrontal cortex was washed with PBS or non-washed. Significance by 2- tailed t-test (CTL vs AD): *$p<0.05$.

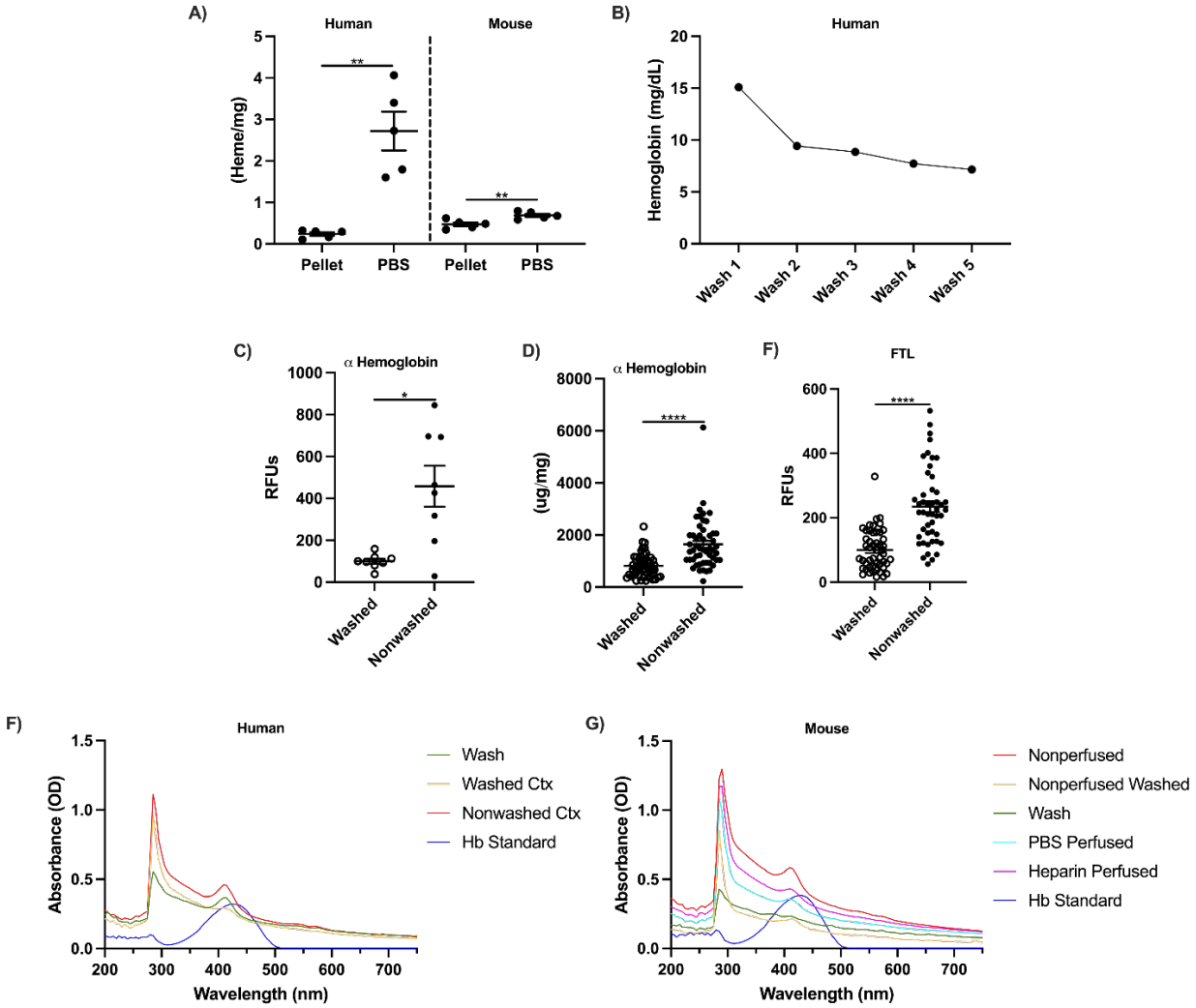

Supplemental Figure 3: A) Nonperfused mouse and human brain tissues were washed to minimize residual blood with PBS and pelleted by centrifugation. **B)** Collected wash was assayed for heme in 5 consecutive washes. Washes 3-5 yielded <10% further decreases. The reduction in α-hemoglobin in human frontal cortex was confirmed by **C)** Western blot, **D)** immunoassay, and **E)** Western blot FTL. Corresponding spectra for hemoglobin at 410 nm confirmed removal for **F)** human and **G)** mouse cortex. Significance by 2- tailed t-test: **p<0.01.

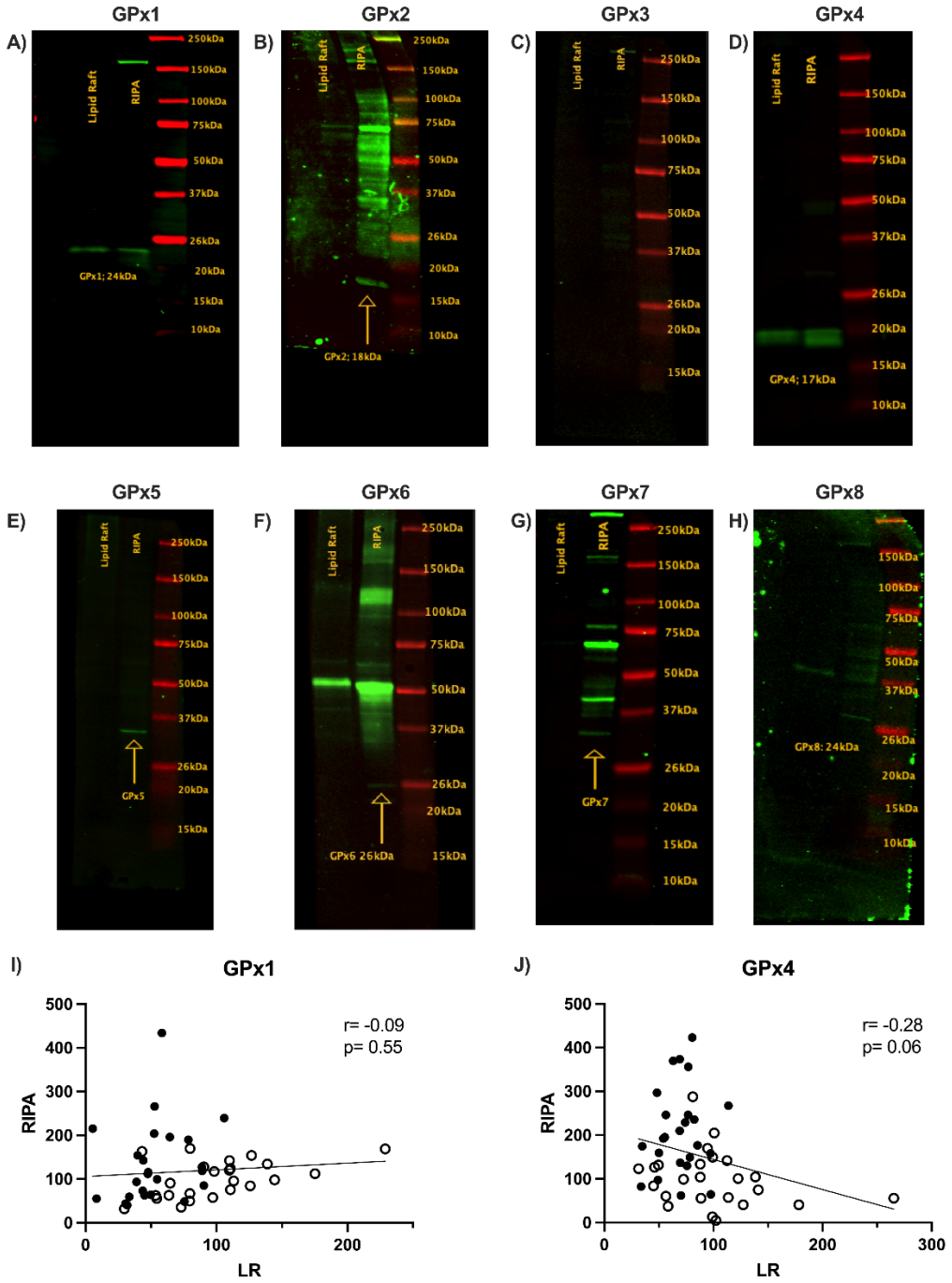

Supplemental Figure 4: Glutathione Peroxidases (GPx) 1 and 4 in lipid rafts from prefrontal cortex. The GPx isoforms of lipid rafts from human prefrontal cortex were immunologically identified by Western blots of lipid raft and whole cell lysates (RIPA buffer extract). **A)** GPx1, **B)** GPx2, **C)** GPx3, **D)** GPx4, **E)** GPx5, **F)** GPx6, **G)** GPx7, **H)** GPx8. Coplots of **I)** GPx1 and **J)** GPx4 for RIPA extract and lipid raft fractions.

Age	Sex	AD Status	Braak	ApoE Allele	PMI (hours)	Frontal Cortex	Cerebellum	MMSE	MMSE Interval (Months)	ADRC
99	Female	CTL	0	3,3	9	x	x	28	23.4	USC
91	Female	CTL	0	3,3	8.75	x	x	20	84	USC
85	Female	CTL	0	3,3	7	x	x	N/A	N/A	USC
95	Female	CTL	1	3,3	3.25	x	x	N/A	N/A	USC
87	Female	CTL	2	3,3	10.75	x	x	29	1	USC
95	Female	CTL	2	3,3	2.92	x	x	N/A	N/A	UCI
86	Female	CTL	3	3,3	6.17	x	x	30	35.5	UCI
90	Female	CTL	3	3,3	2.2	x	x	N/A	N/A	UCI
89	Female	CTL	3	3,3	3.58	x	N/A	24	5.9	UCI
94	Female	AD	4	3,3	10.5	x	x	N/A	N/A	USC
81	Female	AD	5	3,3	7.5	x	x	N/A	N/A	USC
89	Female	AD	5	3,3	1.5	x	x	N/A	N/A	USC
66	Female	AD	6	3,3	17	x	x	N/A	N/A	USC
70	Female	CTL	1	3,4	4.17	N/A	x	28	20.1	UW
86	Female	CTL	3	3,4	9.33	N/A	x	29	12.3	UW
97	Female	CTL	3	3,4	0	N/A	x	26	6.6	UW
91	Female	CTL	3	3,4	11.2	x	x	23	10.1	UW
85	Female	CTL	3	3,4	4.2	N/A	x	29	37.9	UW
89	Female	CTL	3	3,4	3.5	N/A	x	27	28.7	UW
74	Female	CTL	3	3,4	4.5	N/A	x	30	44.3	UW
91	Female	CTL	3	3,4	3.33	x	x	27	42.5	UCI
87	Female	CTL	3	3,4	4.57	x	x	29	85.6	UCI
93	Female	CTL	5	3,4	4.15	x	x	30	81.6	UCI
81	Female	AD	5	3,4	5.5	x	x	N/A	N/A	USC
84	Female	AD	5	3,4	6	x	x	N/A	N/A	USC
80	Female	AD	5	3,4	19	x	x	N/A	N/A	USC
96	Female	AD	6	3,4	9	N/A	x	N/A	N/A	USC
77	Female	AD	6	3,4	8.25	x	x	N/A	N/A	USC
87	Female	AD	6	3,4	4.5	N/A	x	N/A	N/A	USC
78	Female	AD	4	4,4	15.5	x	x	N/A	N/A	USC
81	Female	AD	5	4,4	4	x	x	N/A	N/A	USC
80	Female	AD	5	4,4	3.75	x	x	N/A	N/A	USC
76	Female	AD	5	4,4	5.25	x	x	N/A	N/A	USC
82	Male	CTL	0	3,3	9	x	x	28	N/A	USC
93	Male	CTL	0	3,3	12	x	x	30	1229.2	USC
93	Male	CTL	0	3,3	3.75	x	x	N/A	N/A	USC
76	Male	CTL	0	3,3	11.25	x	x	N/A	N/A	USC
86	Male	CTL	2	3,3	4.42	x	x	25	48.4	UCI
83	Male	CTL	2	3,3	3.18	x	x	N/A	N/A	UCI
86	Male	CTL	3	3,3	2.92	x	x	20	37	UCI
80	Male	CTL	3	3,3	4.05	x	x	26	95.1	UCI
97	Male	AD	3	3,3	5.25	x	x	N/A	N/A	USC
87	Male	AD	4	3,3	4.75	x	x	N/A	N/A	USC
76	Male	AD	5	3,3	9.75	x	x	N/A	N/A	USC
88	Male	AD	5	3,3	6.75	x	x	N/A	N/A	USC
92	Male	CTL	0	3,4	5.25	x	x	N/A	N/A	USC
87	Male	CTL	1	3,4	4	N/A	x	25	8.9	UW
90	Male	CTL	3	3,4	5.8	x	x	N/A	N/A	UCI
97	Male	CTL	4	3,4	5.83	x	x	26	7	UCI
87	Male	CTL	4	3,4	6.28	x	x	22	101.5	UCI
77	Male	AD	2	3,4	6	x	x	N/A	N/A	USC
81	Male	AD	3	3,4	7.25	x	x	N/A	N/A	USC
85	Male	AD	5	3,4	7.25	x	x	N/A	N/A	USC
72	Male	AD	6	3,4	9	x	x	N/A	N/A	USC
75	Male	AD	0	4,4	9.5	x	x	N/A	N/A	USC
88	Male	AD	5	4,4	5	x	x	N/A	N/A	USC
92	Male	AD	5	4,4	8.25	x	x	N/A	N/A	USC
70	Male	AD	5	4,4	3.5	x	x	N/A	N/A	USC
81	Male	AD	5	4,4	6.54	N/A	x	N/A	N/A	USC

Supplemental Table 1: Data provided for brain specimens by each ADRC source: USC, 37; UCI, 14; UW, 8. White, 76%; Latino, 14%; African American, 3%; Asian, 2%; N/A, 5%. ApoE3,3, 42%, ApoE3,4, 42%, ApoE4,4, 16%.

	NFT-Bearing Neurons				**NFT-Free Neurons**		
	NFT	Cytoplasm	Nucleus	Neuropil	Cytoplasm	Nucleus	Neuropil
AD	65 ± 9	20 ± 3	42 ± 5	14 ± 3	12 ± 2*	44 ± 7*	11 ± 1*
CTL	N/A	N/A	N/A	N/A	4 ± 0.5	17 ± 2	4 ± 0.5

Supplemental Table 2: Iron in NFT free and bearing neurons presented as mass charge ratio (m/z) by Good et al. 1992[13]. Significance by 2-tailed t-test: *$p<0.05$.

Measurement	Cortex (AD vs CTL)	Cerebellum (AD vs CTL)	Cortex (ApoE3,3 vs 3,4 & 4,4)	Cerebellum (ApoE3,3 vs 3,4 & 4,4)	Cortex Male (AD vs CTL)	Cortex Female (AD vs CTL)
FTL	+65% **	+10%, n.s.	+30%, n.s.	-30%, n.s.	+55%, n.s.	+75% *
FSP1	-40% ****	-30% ****	-40% *	-20% **	-50%, n.s.	-30% *
GCLM	-60% ****	-35% *	-30%, n.s.	-15%, n.s.	-65% ****	-55% ***
GPx4	+110% ****	-15% *	+45% *	-30, n.s.	+45%, n.s.	+210% ***
GPx4, LR	-30% **	-40% ****	-5%, n.s.	-5%, n.s.	-25% **	-35%, n.s.
Heme	+25% *	+30% **	+5%, n.s.	+10%, n.s.	+20%, n.s.	+25%, n.s.
HNE, Total	+60% ****	-20%, n.s.	+35% **	-25% *	+35% **	+90% ***
HNE, LR	+160% ****	+45% **	+80% **	+35% *	+170% **	+180% ***
NF-κB, nuclear	+175% **	+5%, n.s.	+70%, n.s.	+5%, n.s.	+45%, n.s.	+290% **
Nrf2, nuclear	-75% ****	-15%, n.s,	-65% ***	-15%, n.s.	-85% **	-60% **

Supplemental Table 3: AD change in prefrontal cortex (Brodmann 8-10) and cerebellum by ApoE3 and 4 alleles. FTL, ferritin light chain; FSP1, ferroptosis suppressor protein 1; GPx4, glutathione peroxidase 4. t-test *p<0.05, **p<0.01, ***p<0.001, ****p<0.0001; n.s, not significant, p>0.05.

Extended Figures

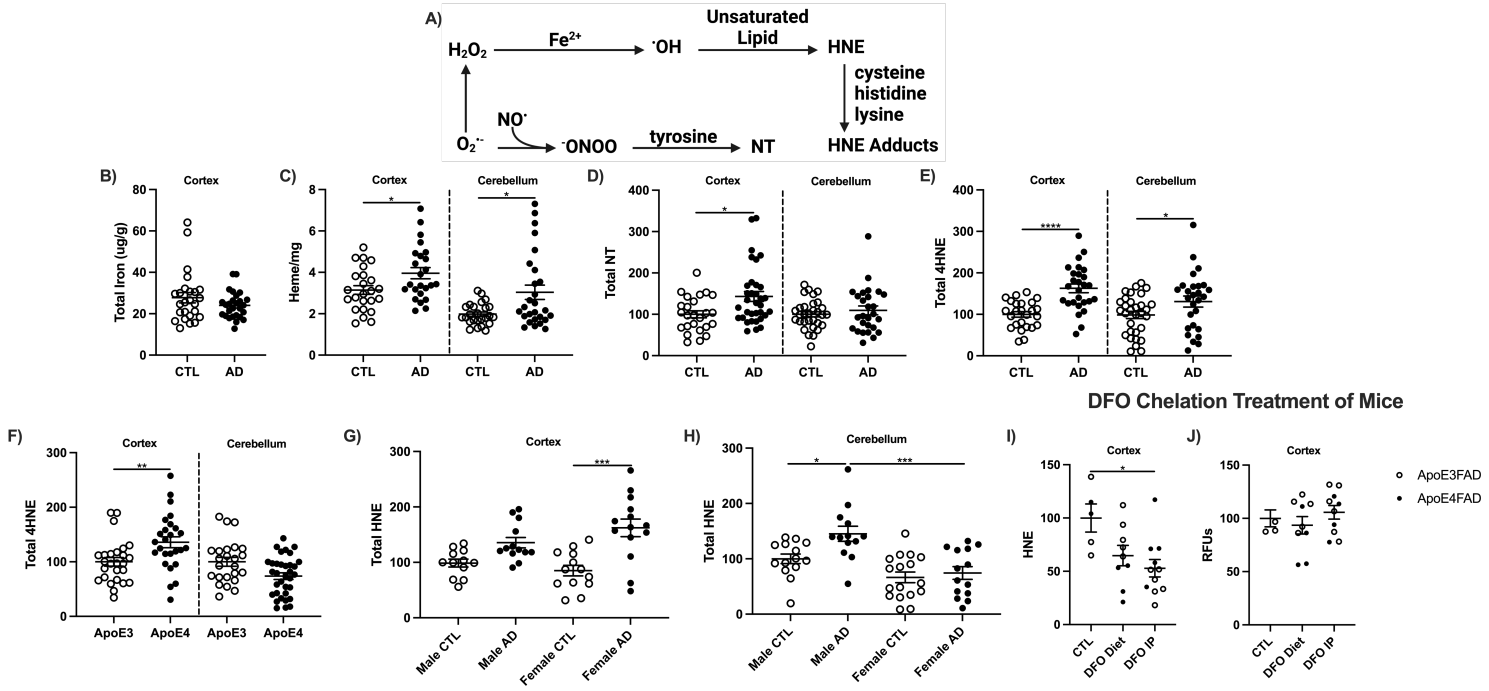

Extended Figure 1: Oxidative damage to prefrontal cortex (n=25-27/group) and cerebellar (n=27-31/group) proteins (HNE, NT) in age matched AD and cognitively normal control (CTL). **A)** Schematic representing oxidative damage to lipids and proteins. Hydroxyl radicals (·OH) are

produced during oxidation of Fe^{2+} or Cu^{+} ('Fenton chemistry') and may oxidize adjacent proteins, lipids or nucleic acids. HNE can alter proteins via Michael addition products through its double-bonded carbons, or by forming Schiff bases through its aldehyde moiety. The bottom reaction shows the iron-independent oxidative pathway to form peroxynitrite $^{-}ONOO$ from $O_2^{\bullet-}$ and $^{\cdot}NO$, which can then oxidize tyrosine to NT. Aggregated human Aβ42 stimulated formation of peroxynitrite which was neurotoxic in vitro[43]. Non-heme iron also mediates lipoxygenase activity[44]. Prefrontal cortex from Brodmann area 8, 9, or 10 and cerebellum was washed measurements for **B)** Total iron, measured by ICP-MS **(Table 1B)**, **C)** heme, and dot blots for **D)** NT, and HNE presented as **E)** cognitively normal vs AD, **F)** ApoE allele, or sex in **G)** cortex or **H)** cerebellum. Dot blots of DFO treated ApoEFAD mouse for **I)** HNE and **J)** NT as relative fluorescent units (RFUs). Significance by 2-tailed t-test: *p<0.05, **p<0.01, ***p<0.001, ****p<0.0001.

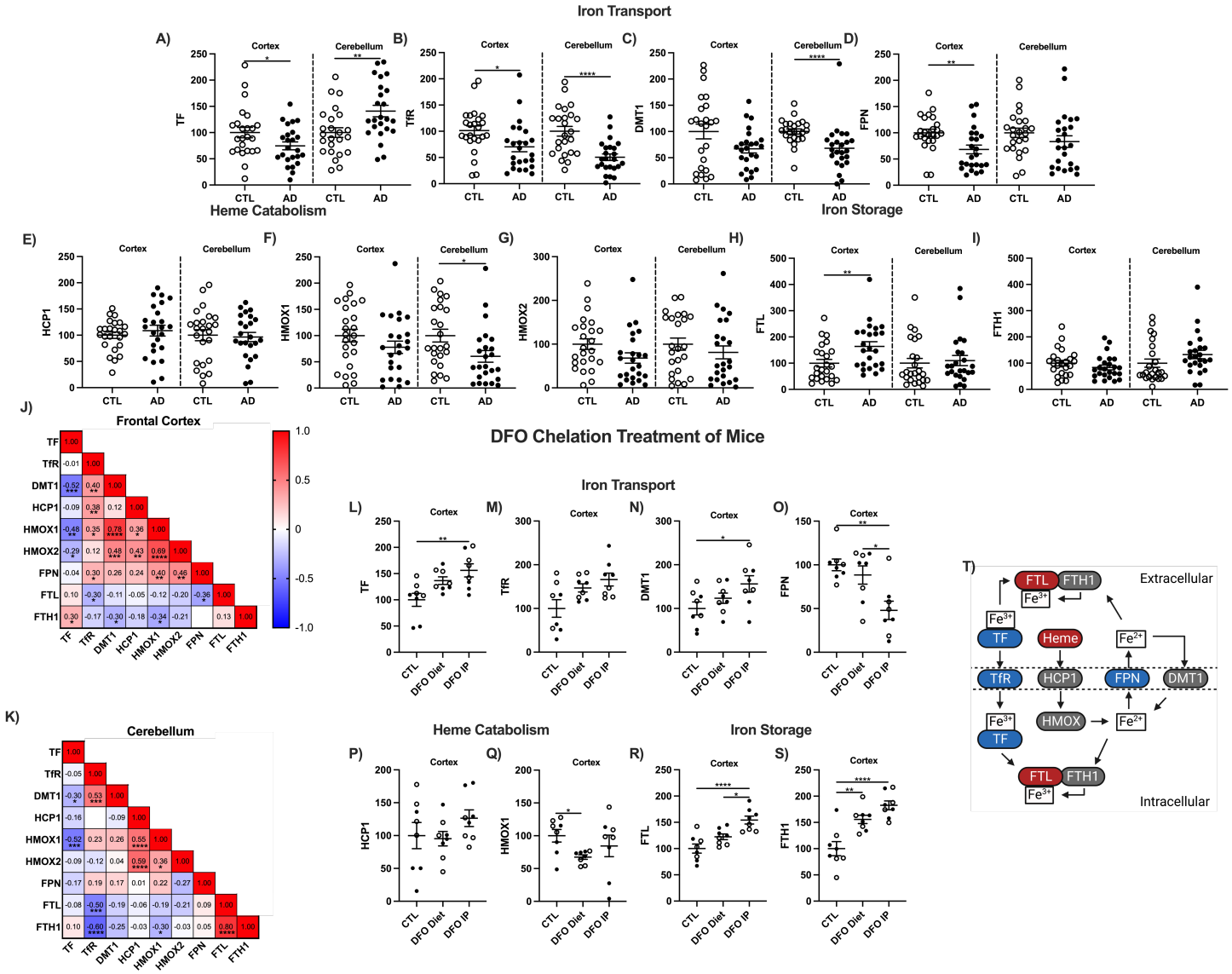

Extended Figure 2: Iron transport and metabolism in AD (n=24) compared to cognitively normal (n=24) for prefrontal cortex and cerebellum. Iron transport and metabolism in AD prefrontal cortex and cerebellum. Relative fluorescent units from Western blots. **A)** transferrin (TF), **B)** transferrin receptor (TfR/CD71), **C**) divalent metal transporter 1 (DMT1), **D)** ferroportin (FPN), **E)**, heme carrier protein 1 (HCP1), **F)** hemeoxygenase 1 (HMOX1), **G)** heme

oxygenase 2 (HMOX2), **H)** ferritin light chain (FTL), **I)** ferritin heavy chain 1 (FTH1), Correlation matrix for iron metabolism in clinical AD for **J)** prefrontal cortex and **K)** cerebellum. Western blots of DFO treated ApoEFAD mice **L)** TF, **M)** TfR, **N)** DMT1, **O)** FPN, **P)** HCP1, **Q)** HMOX1, **R)** FTL, and **S)** FTH1. **T)** Summary of AD changes in prefrontal cortex: blue, decrease; red, increase. Significance, 2-tailed t-test (A-I), Spearman correlation (J,K), or One-way ANOVA with Tukey's posthoc (L-S): *p<0.05, **p<0.01, ***p<0.001, ****p<0.0001.

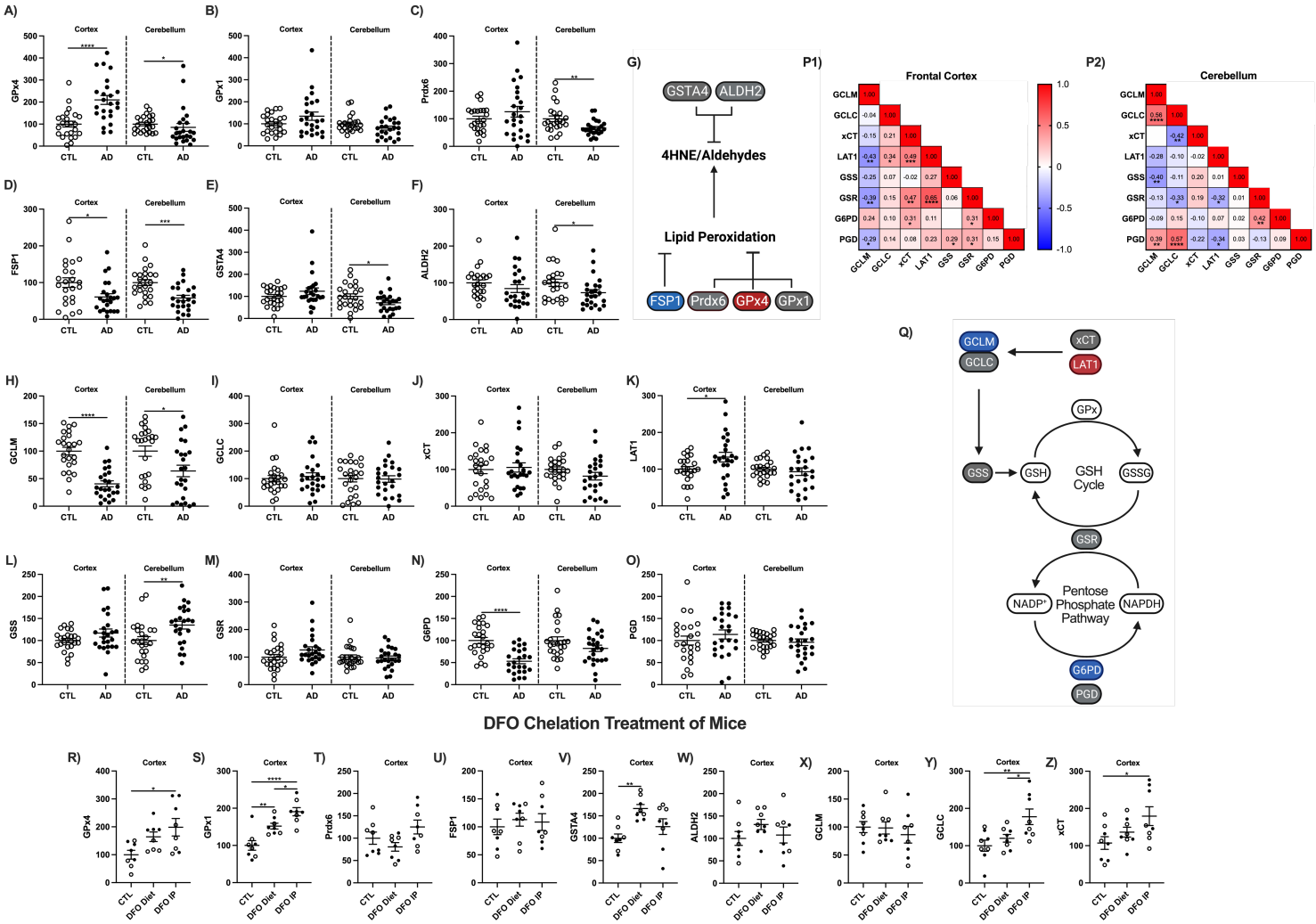

Extended Figure 3: Enzymes that mitigate lipid peroxidation and facilitate GSH production. Western blot data is shown as relative fluorescent units (RFUs) for prefrontal cortex or cerebellum from whole tissue lysate for antioxidants **A)** GPx4, **B)** GPx1, **C)** Prdx6, **D)** FSP1, **E)** GSTA4, and **F)** ALDH2. **G)** Enzymatic repair of lipid peroxidation. GSH cycle enzyme levels by Western blots, as relative fluorescent units (RFU). **H)** GCLM, **I)** GCLC, **J)** xCT/SLC7A11, **K)** LAT1, **L)** GSS, **M)** GSR, **N)** G6PD, and **O)** PGD. Correlation matrix for GSH cycle enzymes for **P1)** prefrontal cortex **P2)** cerebellum and **Q)** Schema of GSH metabolic enzymes and pentose phosphate pathway. AD increase (red), decrease (blue), no change (grey), relative to cognitively normal controls; not measured (white). Western blots of DFO treated ApoEFAD mouse cortex for **R)** GPx4, **S)** GPx1, **T)** Prdx6, **U)** FSP1, **V)** GSTA4, **W)** ALDH2, **X)** GCLM, **Y)** GCLC, and **Z)** xCT/SLC7A11. Significance by 2-tailed t-test (A-F, H-O), Spearman correlation (P), or One-way ANOVA with Tukey's posthoc (R-Z): *p<0.05, **p<0.01, ***p<0.001, ****p<0.0001.

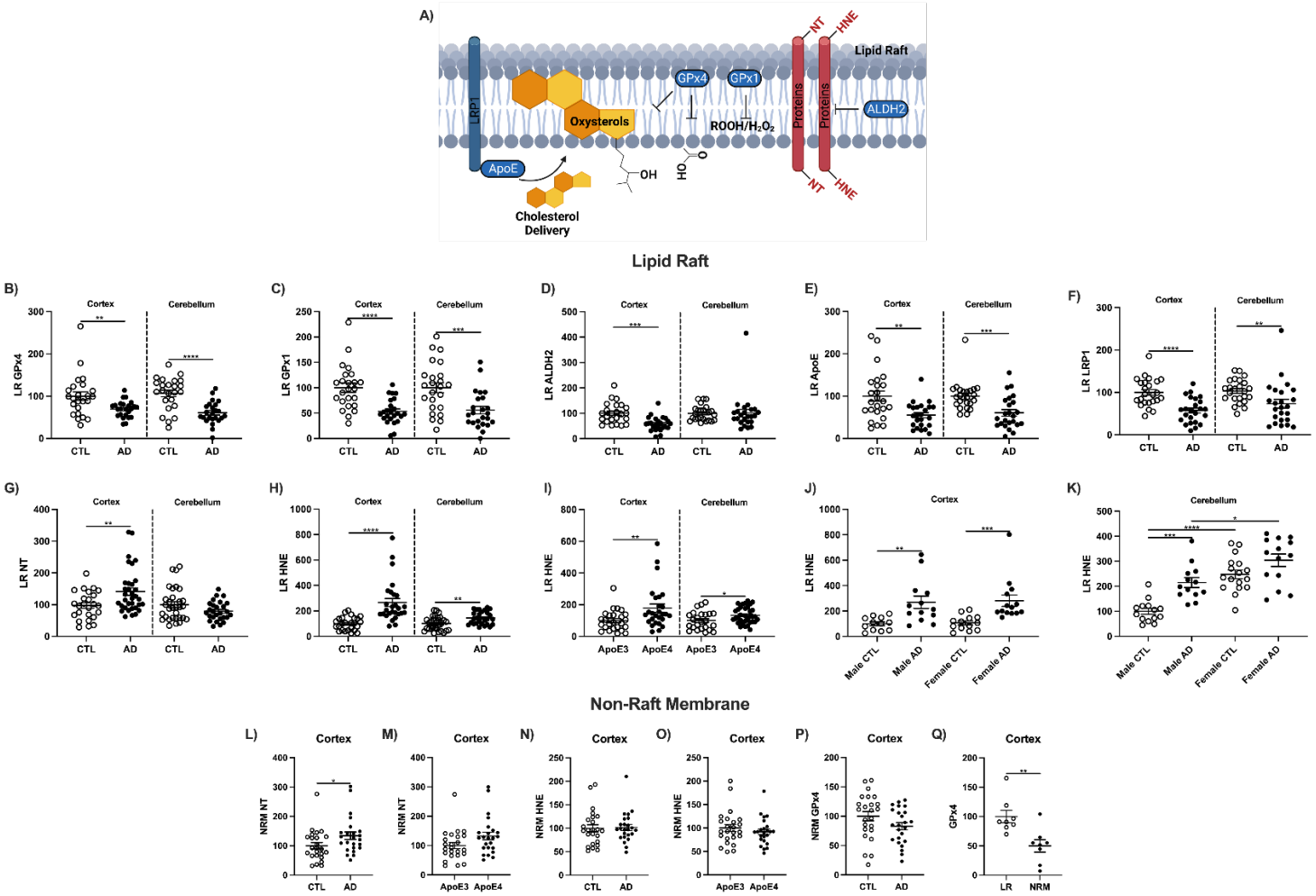

Extended Figure 4: A) Schema of lipid raft damage, protective mechanisms, and cholesterol shuttling in AD prefrontal cortex and cerebellum. Western blots (n=24/group) as relative fluorescent units (RFUs) of lipid raft **B)** GPx4, **C)** GPx1, **D)** ALDH2, **E)** ApoE, **F)** LRP1. Dot blots (n=25-27/group) for **G)** NT, and HNE presented as **H)** CTL vs AD, **I)** ApoE allele, and **J,K)** sex. Non raft membrane dot blots for NT by **L)** CTL vs AD and **M)** ApoE allele, HNE presented as **N)** CTL vs AD or **O)** ApoE allele. Western blot of **P)** NRM GPx4 and the **Q)** comparison of GPx4 in LR vs NRM of cognitively normal ApoE3,3. B-I, L-Q) Significance by 2-tailed t-test or J,K) one-way ANOVA with Tukey's posthoc: *p<0.01, **p<0.01, ***p<0.001, ****p<0.0001.

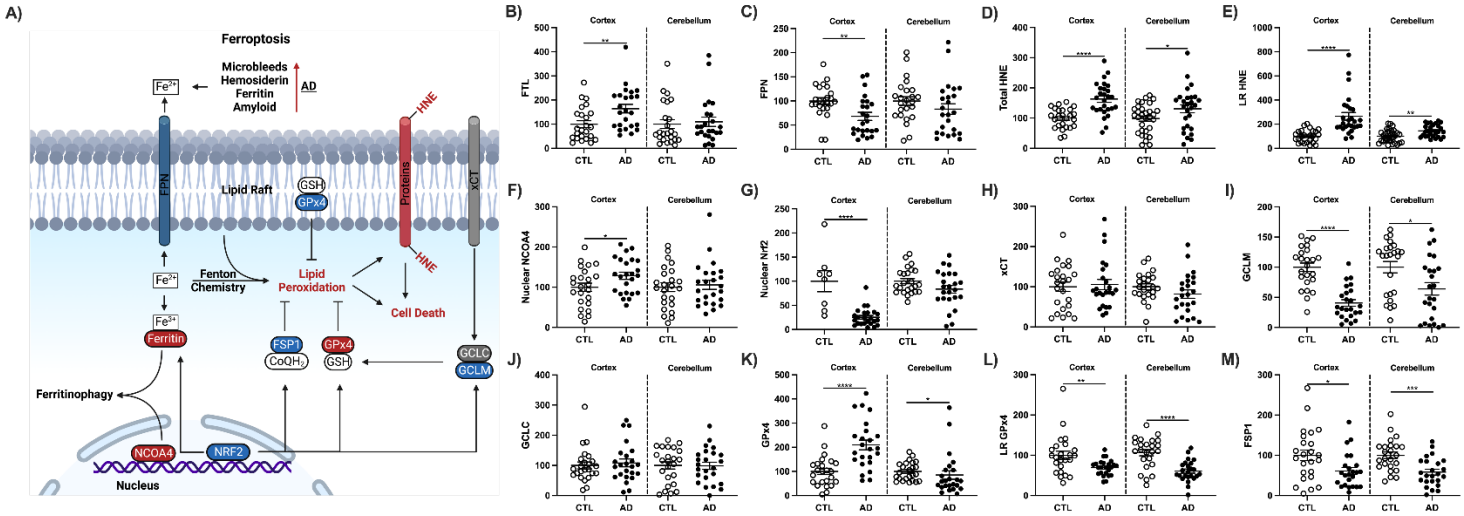

Extended Figure 5: Ferroptosis schema which consolidates data from prior figures. **A)** Schema of ferroptosis markers related to iron transport, lipid rafts, and oxidative damage mitigation. **B)** FTL, **C)** FPN, **D)** HNE, **E)** lipid raft HNE, **F)** NCOA4, **G)** Nrf2, **H)**, xCT, **I)**, GCLM, **J)** GCLC, **K)** GPx4, **J)** Lipid raft GPx4, and **M)** FSP1. Significance by 2-tailed t-test: *p<0.05, **p<0.01, ***p<0.001, ****p<0.0001.

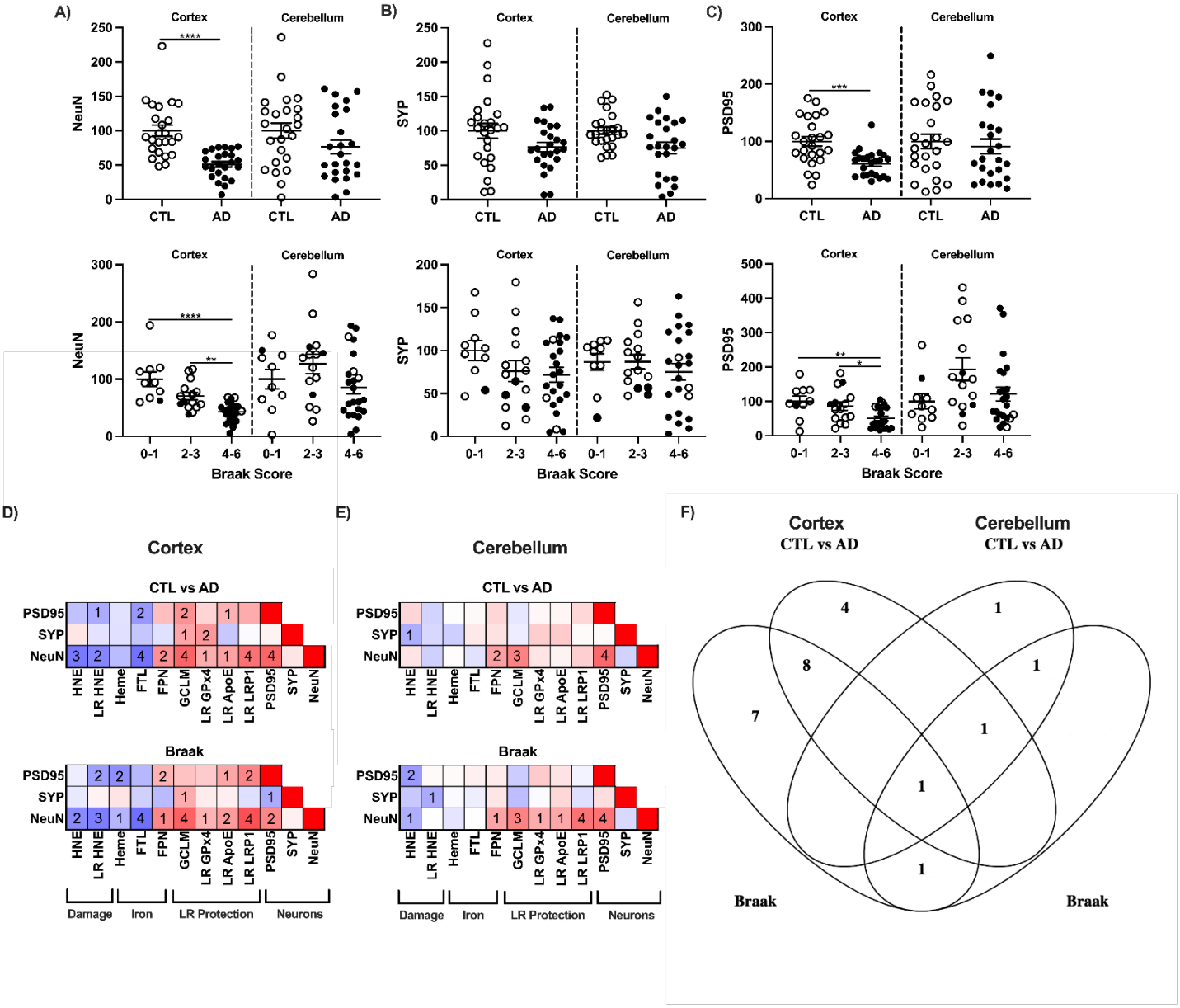

Extended Figure 6: Neuronal loss in AD. Western blots as relative fluorescent units (RFU) of neuronal markers presented as CTL vs AD or Braak stage[34]. **A)** neuronal nuclei antigen (NeuN), **B)** synaptophysin 1 (SYP), **C)** postsynaptic density protein 95 (PSD95). Correlation matrixes for variables with significant relationships to NeuN for **D)** prefrontal cortex and **E)** cerebellum. **F)** Venn diagram comparison of correlations observed in both brain region. Significance by 2- tailed t-test (CTL vs AD), one way ANOVA (Braak) with Tukey's posthoc, or by Spearman correlation: *p<0.05, **p<0.01, ***p<0.001, ****p<0.0001. Correlation matrix: 1, p<0.05; 2, p<0.01; 3, p<0.001; 4, p<0.0001.

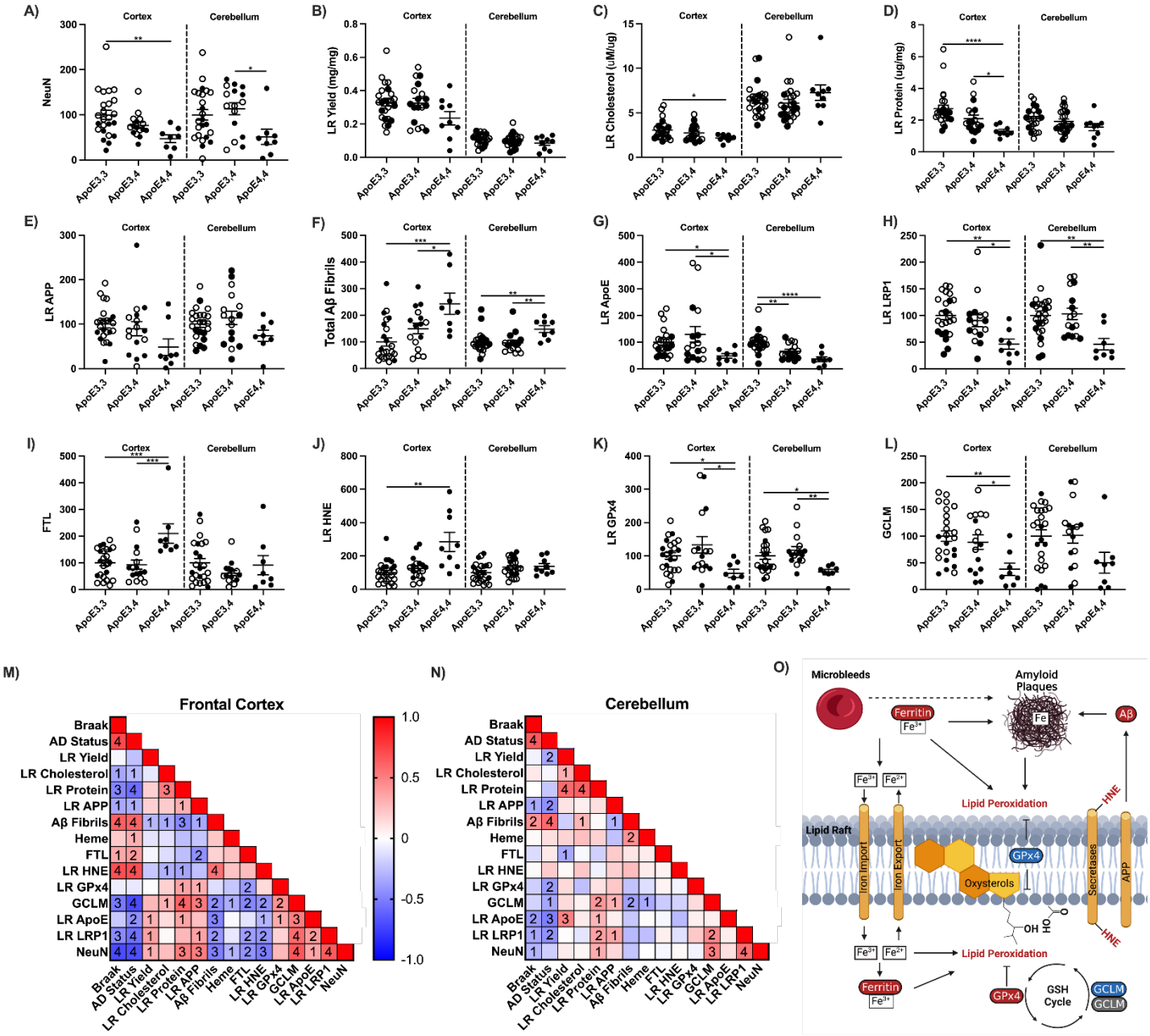

Extended Figure 7: ApoE allele differences are associated with lipid rafts, antioxidant defense, and amyloid. Levels of **A)** NeuN, **B)** LR yield, **C)** LR cholesterol, **D)** total LR protein, **E)** LR APP, **F)** total Aβ fibrils, **G)** LR ApoE, **H)** LR LRP1, **I)** FTL, **J)** LR HNE, **K)** LR GPx4, and **L)** GCLM in prefrontal cortex and cerebellum of cognitively normal (open circles) and demented (closed circles). Correlation matrix of proteins analyzed by ApoE allele in **M)** frontal cortex and **N)** cerebellum. **O)** Hypothesis linking oxidized lipid rafts to amyloid processing. One way ANOVA with Tukey's posthoc, or by Spearman correlation: *p<0.05, **p<0.01, ***p<0.001, ****p<0.0001. Correlation matrix: 1, p<0.05; 2, p<0.01; 3, p<0.001; 4, p<0.0001.

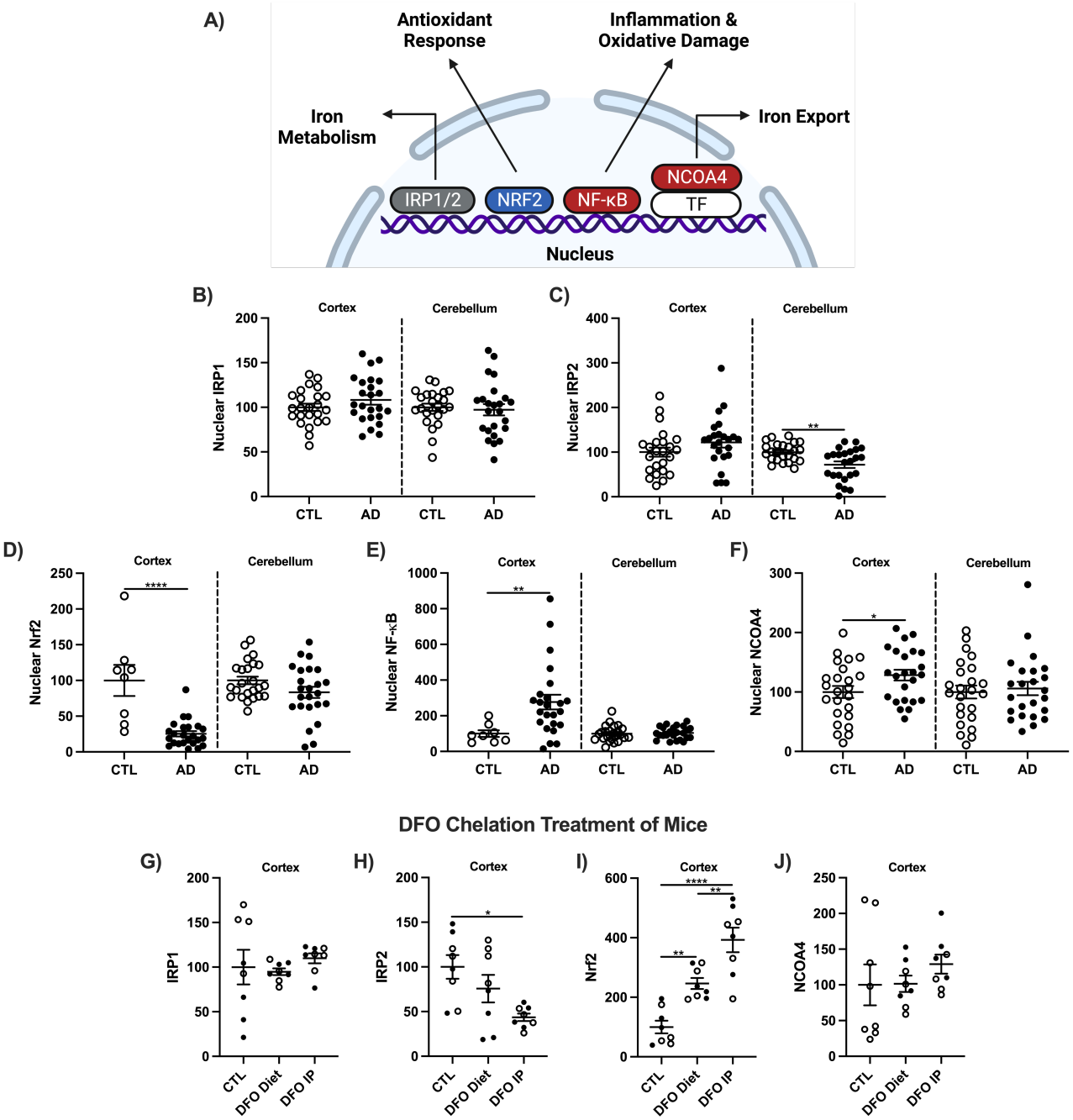

Extended Figure 8: A) Transcription factors of genes for antioxidant defense and iron signaling in human prefrontal cortex of AD and CTL. IRP, iron regulatory protein; Nrf2, nuclear factor erythroid 2–related factor 2; NF-κB p65, nuclear factor κ-light-chain-enhancer of activated B cells; NCOA4, nuclear receptor coactivator 4; TF, transcription factor. Western blot data is relative fluorescent units (RFU) for nuclear **B)** IRP1, **C)** IRP2, **D)** Nrf2, **E)** NF-κB p65, and **F)** NCOA4 in prefrontal cortex and cerebellum and total (RIPA lysate) **G)** IRP1, **H)** IRP2, **I)** Nrf2, and **J)** NCOA4 in DFO treated EFAD mice. B-F Significance by 2-tailed t-test, G-J One way ANOVA with Tukey's posthoc: *p<0.05, **p<0.01, ****p<0.0001.

DISCUSSION:

Iron is increasingly implicated in brain oxidative damage during AD[4,11,12], but the sources of iron and contributions to region-selective neurodegeneration during AD remain unresolved. Ferritin protein was strongly correlated with membrane oxidation (increased HNE) and loss of neurons and synapses

in AD prefrontal cortex. These data were obtained with minimization of blood in the vasculature. We addressed the confound of vascular blood in frozen samples from unperfused human brains by a simple washing procedure. Besides iron, erythrocytes contain ferritin (FTL and FTH1) and GSH enzymes including GPx4 which were decreased by deferoxamine, an iron chelator.

Washed brains from AD and controls had the same levels of total iron in prefrontal cortex. The higher heme in AD than controls by 23% (**Fig 1C**) may arise from leakage of the blood brain barrier or microbleeds [45,46]. Because the washing procedure cannot completely remove intravascular blood, these data should be considered upper limits to heme and ferritin from microbleeds, stroke, and superficial siderosis. The number and size of microbleeds, brain location, and size differ 10-fold between studies[47–50], possibly due to differences in methodology and diversity of clinical samples. Artifactual microbleeds can arise postmortem and may confound correlations of PET imaging for microbleeds with postmortem analysis[51]. Because microbleeds arise sporadically during 'usual aging' as well as in clinical AD, their contribution to brain iron is undefined. Mice transgenic for familial AD genes have increased hemoglobin from microbleeds by age 6-months[50,52] when AD pathology manifests[53]. Microbleed numbers also correlate with Aβ load[52]. Microbleeds and associated hemosiderin deposits may be major sources of total iron in AD brains.

Ferritin deposits store ferric iron which is converted from ferrous iron by ferroxidase in FTH1 [54]. FTL was increased 50% in AD prefrontal cortex. Plaques and NFT contain ferritin protein and multivalent iron[11,55–57]. In addition to its redox activity, iron can modify aggregation of amyloid peptides[58]. Iron also directly influences amyloid peptide production by the iron-response element in the APP primary transcript[59]; moreover, iron can enhance alpha-secretase cleavage[60]. Ferric iron also promotes NFT aggregation, whereas NFTs are solubilized by ferrous iron[61]. Furthermore, neurite dystrophy occurs near amyloid plaques, facilitating microtubule disruption[62]. Hippocampal CA1 neurons that contain NFTs have 2-fold higher iron than the same-cell cytoplasm, shown by laser-guided mass spectrometry[13]. Neighboring CA1 neurons without NFT had 50% less cytoplasmic iron (**Supplemental Table 2**). Given the association of heme with HNE shown here, we predict that NFT-containing neurons have elevated HNE. The hippocampus merits cell-by-cell analysis of HNE in relation to NFT, particularly for the most AD vulnerable CA1 neurons.

Little is known of brain cell types for AD changes in proteins related to iron transport and membrane oxidation. Microglia have high levels of ferritin in AD that are presumed to be phagocytosed from amyloid plaques and NFT[57,63,64]. Endogenous cell ferritin merits consideration because microglia and astrocytes in young rat brain have 2-fold more ferritin than neurons, while oligodendroglia have the highest ferritin levels[65] that may contribute to white matter degeneration during AD in hippocampus and cerebral cortex[26]

Relationships of neurodegeneration to increased brain iron included increased FTL, a major protein of ferritin in senile plaques and NFT. Moreover, AD decreased the four main iron transport proteins: transferrin (TF), its receptor TfR, divalent metal transporter 1 DMT1, and ferroportin FPN. The 40% decrease of FSP1 was consistent with the increased HNE and FTL in AD. Oxidative damage was shown by downstream markers of HNE and NT in association with 2-fold higher GPx4 in prefrontal cortex.

Lipid rafts, the site of neuronal amyloid peptide production, also showed increased oxidative damage and reduced repair in AD brains while the non-raft membrane fraction showed minimal AD change, suggesting that lipid rafts may be hotspots for iron mediated oxidative damage. Paralleling whole brain tissue, lipid rafts from prefrontal cortex had 50% higher HNE in AD. However, unlike its increase in whole tissue of prefrontal cortex, lipid raft GPx4 was 50% lower, suggesting lipid rafts may be more vulnerable for oxidative damage during AD. Furthermore, baseline GPx4 is 2-fold higher in lipid rafts of normal brains than in the non-raft membrane fraction. Cytosolic GPx4 is 20kDa, while the 23kDa isoform with a leader sequence is cleaved after mitochondrial import[66]. Because lipid rafts are derived from all brain cells, the loss of GPx4 may include mitochondrial membranes; alternatively, leader sequences may be needed for membrane localization. Lipid raft composition from prefrontal

cortex was defined for glutathione peroxidases (GPx1-8) and contained only GPx1 and GPx4 but not Prdx6, also essential to membrane repair of lung and epithelial cells[67,68]. The absence of Prdx6 in the lipid raft fraction is consistent with its transient interactions with membranes[69,70]. Prdx6 and GPx1 also reduce lipid hydroperoxides[71] released from membrane lipids[72] and may therefore play a secondary role in defense against ferroptosis.

Oxidation may enhance APP processing by the secretases, shown for γ-secretase in rat cortex neurons and human neuronal cells exposed to 1-10 μM HNE or 100 μM $FeSO_4$[73]. Moreover, H_2O_2 increased BACE1 activity in mouse neuronal N2a cells transgenic for human APP_{695}[74]. Oxidizable amino acids that can be conjugated by HNE and NT are abundant in APP processing enzymes BACE1 (57/501) or PSEN1 (50/467), while ADAM10 (142/748) has 3-fold more vulnerable residues. BACE1 activity increases with AD in prefrontal cortex[75]. Recognizing that HNE and NT can increase or decrease enzyme activities [74,76], biochemical analysis is needed for secretase activity in relation to membrane oxidation in AD brains. The decreased NeuN and the lower yield of lipid rafts shown by us[34] from AD in prefrontal cortex, but not cerebellum, is consistent with the regional specificity of neurodegeneration. The concurrent loss of neurons, decreased lipid raft yield, and increased membrane oxidation are correlated with fibrillary amyloid. AD increases of BACE1 activity in brain and serum[77,78] parallel the increased peroxidation of serum and tissue lipids[79,80].

The ApoE4 allele, a major AD risk factor, is associated with higher HNE in prefrontal cortex but not cerebellum. Whole tissue and lipid raft HNE in prefrontal cortex were higher in E4 carriers than E3, while NT did not differ by ApoE allele. ApoE4 prefrontal cortex had 35% higher HNE than E3; the absence of E4 differences in cerebellum correspond to its lesser AD neurodegeneration. The E4 allele was also associated with less FSP1 and nuclear Nrf2 in prefrontal cortex which protect against oxidative damage. The current sample of 52 brains is underpowered to evaluate differences by ApoE allele-sex interactions.

The transcription factor Nrf2 induces phase II gene response that mitigate oxidative damage including GPx4[81,82]. Nrf2 mediated antioxidant defense declines with age in cells and tissues including cerebellum[83,84]. We suggest that the age-related decline of Nrf2 defense facilitates higher membrane oxidation and amyloid peptide production (**Fig. 7N**). Increased nuclear p65 NF-kB may inhibit Nrf2 gene response[85,86] because both require binding of the CBP/P300 transcriptional co-activators[86]. The 3-fold increases in nuclear p65 NF-κB in AD suggest increased activity of genes that promote oxidative damage (**Fig.1)**.

Genomic damage during AD involves iron-derived oxidants. Heme from microbleeds and microhemorrhages may contribute to oxidants via iron from heme degradation by heme oxygenases[87]. AD brains have 2-fold increased double-strand DNA breaks (DSB) in neurons and astrocytes[88]. The link of iron to DSBs in neurons was shown experimentally with chelation of iron by deferoxamine[22], which decreased DSB in mice injected with hemolyzed blood and in cultured neurons exposed to hemin. Unspecified oxidative damage is implied for exomic somatic mutations in the AD hippocampus with the 'oxidative mutational signature' C>A[89]. Iron is given little attention in the growing literature of genomic instability in AD.

Chelation therapy for AD was first attempted in 1991 to remove aluminum by deferoxamine (DFO), which slowed cognitive decline in subjects during 24-months[90]. While cognitive benefits were attributed to chelation of brain aluminum, Gleason and Bush[91] noted that DFO has 6-fold greater affinity for ferric iron than aluminum, which implies that cognitive improvements were due to iron chelation, rather than aluminum. Contrary to a common understanding that DFO cannot cross the BBB, tritiated (H^3) DFO was 3-fold higher per gram tissue in dog brain than plasma and kidney[92] and has similar efficacy to other chelators[93,94]. In the present EFAD mouse studies with DFO the increase in brain iron transport and storage proteins, together with the decreased iron export protein FPN suggests a homeostatic response to retain intracellular iron. This increases did not differ by ApoE allele. Furthermore, the decrease of HNE by DFO shows the reversibility of iron mediated lipid

peroxidation in brain suggesting iron chelation may be beneficial for neurodegenerative diseases involving lipid peroxidation.

The present human brains also did not differ by aluminum for AD vs CTL (**Supplemental Fig. 2**). This early chelation study was not pursued because of weakening evidence for the environmental role of aluminum, despite growing evidence for the role of iron in amyloid aggregation. Decades later, a new chelation trial has begun, 'Deferiprone to Delay Dementia'. The '3D Study' (NCT03234686) is a randomized study of prodromal and mild AD patients by ApoE genotype for cognition and brain iron levels, with expected completion by September 2023. Whatever is learned from the 3D Study, future therapies may consider chelation in combination with amyloid removal and include direct measures of brain synapse density by PET. Little is known about the turnover of iron in plaque or NFT. A new concern arises: do monoclonal therapies that decrease amyloid plaque size also cause by-stander damage from released redox active iron?

Air pollution may also enhance iron-mediated neurodegeneration, suggested by ferritin deposits in the olfactory bulb that are contiguous with foreign particulate material[95]. Connections of the olfactory pathways throughout the brain merit analysis for iron-associated damage from air pollution. For example, air pollution derived nanoparticles (nPM) caused membrane oxidation in lipid rafts in an ADtg mouse[96]. Acute exposure to nPM rapidly increased HNE and NT in mouse olfactory bulb in wildtype mice[97].

In summary, this analysis of iron metabolism and membrane oxidation in AD is the first to comprehensively document the ensemble of 20 proteins that mediate iron transport and GSH-mediated neuroprotection. AD pathway specificity was shown by the greater change in prefrontal cortex than cerebellum consistent with their associated AD neuropathology. Prior studies on subsets of these proteins had lower statistical strength from smaller sample size. These data substantiate reports of lipid peroxidation during AD (see introduction), and identify novel alterations in iron related transport, clearance, and oxidative repair mechanisms. Experimental reduction of lipid peroxidation in mice by iron chelation may be considered for co-therapy with monoclonal antibody treatments to reduce amyloid that inevitably release iron associated with amyloid plaques. Taken together, this suite of findings supports the concept of ferroptosis during AD. Future studies will analyze neuronal and glial membrane damage in relation to the cellular localization of iron deposits in brain pathways from the prefrontal cortex to the hippocampus. Lastly, iron chelation may be useful for treatment of neurodegenerative conditions in combination with amyloid monoclonal therapies.

METHODS:

Human Samples Postmortem prefrontal cortex and cerebellum with Braak scores were provided by three Alzheimer's Disease Centers: University of Southern California (Dr. Carol Miller), University of California Irvine (UCI MIND), and University of Washington (BRaIN). Samples were genotyped for ApoE alleles by PCR for SNP variants rs429358 and rs7412. All human subjects provided informed consent. Human tissue use was approved through IRB protocol #UP-20-00014-EXEMPT. Details for individual brains are in **Supplementary Table 1**.

Mice C57BL/6 mice from Jackson laboratories or ApoEFAD mice from Mary Jo LaDu (University of Illinois, Chicago) were housed by the University of Southern California's Department of Animal Resources. Mice had ad libitum access to Purina Lab Chow (LabDiet, Hayward, CA) and water. Mice were housed in groups of 5 at 22°C/ 30% humidity, with standard nesting material and light cycles of 0600-1800 hr. Studies were approved by the USC Animal Use and Care Committee (IACUC# 20417). Female ApoEFAD mice were given DFO treatment either in rodent chow (10mg/kg/day) for two weeks or by intraperitoneal injection twice daily for one week (10m/kg/day). At 6-month old mice were anesthetized with isoflurane and euthanized by cardiac puncture. C57BL/6 mouse cortex was collected as non-perfused, with transcardial PBS perfusion, or PBS perfusion + 10U/mL heparin (Sigma-Aldrich, St. Louis, MO). Tissues were stored at -80°C.

Tissue Washing Human and mouse brain tissue was thawed on ice and minced with surgical scissors for heme or ceramic scalpel for iron measurements. PBS (10 volumes) was placed in each tube and the samples were gently washed by two cycles of vortexing and collected by gentle centrifugation 800g/30 sec/4°C. PBS was retained on a small subset of samples and further spun at 4,000g/10 min/ 4°C. The pellet was sonicated 10 sec at 50% power in PBS. Resuspended pellet and lysate were assayed for heme (**Table 1; Supplemental Fig. 3**).

Amyloid Measurements Human tissue was processed for amyloid measurements as previously described. Briefly, tissue was homogenized in RIPA without SDS and spun for 10,000g for 1h at 4°C. Supernatant was collected and analyzed for soluble Aβ fibrils using M78 (Conformation specific antibody for Aβ fibrils[98], a gift from Dr. Charles Glabe, UCI). The residual pellet was resuspended in 70% formic acid and sonicated. The resuspension was nutated at room temperature for 2h and neutralized with 20 volumes of 1M Tris and concentrated with a vacuum concentrator (Labconco, Kansas City, MO).

Lipid Raft and Non-Raft Membrane The lipid raft fraction was isolated from 40 mg homogenates of frozen prefrontal cortex (Brodmann area 8, 9 or 10) and cerebellum using a column-based isolation kit (Invent Biotechnologies, Plymouth, MN). These findings were verified by sucrose gradient ultracentrifugation[96]. Lipid raft and the remaining detergent soluble non-raft membrane (NRM) fractions were resuspended in PBS+1% triton x-100 and sonicated 10 seconds at 50% power. Protein was assayed by the copper-based 660 nm assay (ThermoFisher Scientific, Waltham, MA). Lipid raft enrichment and purity were determined by cytosolic GAPDH, lipid raft marker flotillin1, and nuclear marker H3[34].

Nuclear Isolation 20 mg frozen brain was homogenized in 125uL of sucrose buffer for nuclear and cytosolic fractions . The protocol[101] was modified for brain tissue by adding 1% NP-40 to the first wash step, resuspending the pellet, and incubating on ice for 30 min. Nuclear and cytosolic extractions were cross probed for purity against both H3 and GAPDH by Western blot[100] and showed the expected distribution (**Supplemental Fig. 1**).

Western Blot Proteins from lipid rafts (5 ug), whole cell lysate (20 ug), or nuclear fractions (20 ug) were boiled at 75°C under denatured conditions and resolved on 4-20% gradient gels. Proteins were electroblotted using a Criterion blotter (Bio-Rad Laboratories, Hercules, CA) and transferred onto 0.45um polyvinyl difluoride membranes. Membranes were stained using Revert 700 fluorescent protein stain and imaged prior to blocking with LI-COR Intercept blocking buffer (LI-COR Biosciences, Lincoln, NE), followed by primary antibodies. Membranes incubated with IRDye 800CW and/or 700CW secondary antibodies and visualized by Odyssey (LI-COR Biosciences). Western blot data was quantified with ImageJ and normalized by total protein per lane and/or loading control protein.

Biochemical Assays Lipid rafts were assayed for total cholesterol (Cell Biolabs, San Diego, CA). Tissue hemoglobin or heme quantified by Quantichrom assay (BioAssay Systems, Hayward, CA). α-Hemoglobin was quantified by ELISA (ThermoFisher Scientific, Waltham, MA).

ICP-MS 50mg of brain tissue was cut with a ceramic scalpel and placed in metal free test tubes. Tissue was washed twice with PBS and homogenized with sterilized disposable plastic pestles in Chelex 100 (sigma, St. Louis, MO) with purified water (18.2 MΩ; Millipore, Burlington, MA). Homogenates were desiccated by vacuum centrifuge at 95°C for 90 min. and solubilized in trace metal free 70% HNO_3 overnight. 30% H_2O_2 was then added followed by drying under heat. After resuspension in 2% HNO_3, samples were analyzed by Agilent 7500ce ICP-MS in hydrogen mode with a practical detection limit of

10ppb and a relative standard deviation (RSD) of replicate measures between 0.2 to 5%. Total iron concentration was normalized to wet weight tissue.

Statistics GraphPad Prism 9 software (GraphPad, San Diego, CA) was used for graphing and statistical analysis. Two-tailed t-test or one-way ANOVA with Tukey's HSD ($p<0.05$) were utilized with a confidence interval set at 95%. Data that were not normally distributed were analyzed by Mann Whitney U or Kruskal-Wallis with Dunn's test. All correlation matrixes used Spearman's correlation for non-linear data.

Acknowledgements & Funding
The authors are grateful to Liying Zhao for performing ICP-MS measurements. The authors appreciate the helpful discussions of brain samples with Carol Miller (USC) and C. Dirk Keene (UW). The authors thank Christian J. Pike for helpful discussions. Tissue for this study was obtained from the USC ADRC Neuropathology Core, NIAAG066530. The UCI-ADRC is funded by NIH/NIA Grant P30AG066519. J. Silva and E. Head were supported by P30AG066519. Lab studies were supported by NIH grants to CEF (R01-AG051521, P50-AG05142, P01-AG055367) and Cure Alzheimer's Fund. Brain specimens were obtained from ADRC Tissue Cores: USC (P50-AG005142,AG066530); University of California Irvine (P30-AG066519);UW(P30-AG066509;U01-AG006781). Venn diagrams were made with Venny 2.1.0 and schematics made using BioRender.

Ethics Declarations
All of the authors declare no competing interests.

Data Availability
The authors declare that the data supporting the findings of this study are available within the paper and its Supplementary Information files. Should any raw data files be needed in another format they are available from the corresponding author upon reasonable request.

References
1. Boyle, P. A. *et al.* To what degree is late life cognitive decline driven by age-related neuropathologies? *Brain* **144**, 2166–2175 (2021).

2. Robinson, J. L. *et al.* The development and convergence of co-pathologies in Alzheimer's disease. *Brain* **144**, 953–962 (2021).

3. Goodman, L. Alzheimer's disease; a clinico-pathologic analysis of twenty-three cases with a theory on pathogenesis. *J Nerv Ment Dis* **118**, 97–130 (1953).

4. Ayton, S. *et al.* Regional brain iron associated with deterioration in Alzheimer's disease: A large cohort study and theoretical significance. *Alzheimer's & Dementia* **17**, 1244–1256 (2021).

5. Dixon, S. J. *et al.* Ferroptosis: an iron-dependent form of nonapoptotic cell death. *Cell* **149**, 1060–1072 (2012).

6. Hochstein, P., Nordenbrand, K. & Ernster, L. Evidence for the involvement of iron in the ADP-activated peroxidation of lipids in microsomes and mitochondria. *Biochem Biophys Res Commun* **14**, 323–328 (1964).

7. F, U., M, M., M, V., L, F. & C, G. Purification from pig liver of a protein which protects liposomes and biomembranes from peroxidative degradation and exhibits glutathione peroxidase activity on phosphatidylcholine hydroperoxides. *Biochimica et biophysica acta* **710**, (1982).

8. Minotti, G. & Aust, S. D. The role of iron in the initiation of lipid peroxidation. *Chem Phys Lipids* **44**, 191–208 (1987).

9. Ursini, F., Maiorino, M. & Gregolin, C. The selenoenzyme phospholipid hydroperoxide glutathione peroxidase. *Biochim Biophys Acta* **839**, 62–70 (1985).

10. Lovell, M. A., Robertson, J. D., Teesdale, W. J., Campbell, J. L. & Markesbery, W. R. Copper, iron and zinc in Alzheimer's disease senile plaques. *J Neurol Sci* **158**, 47–52 (1998).

11. Everett, J. *et al.* Biogenic metallic elements in the human brain? *Sci Adv* **7**, eabf6707 (2021).

12. Zeng, Y., DiGiacomo, P. S., Madsen, S. J., Zeineh, M. M. & Sinclair, R. Exploring valence states of abnormal mineral deposits in biological tissues using correlative microscopy and spectroscopy techniques: A case study on ferritin and iron deposits from Alzheimer's disease patients. *Ultramicroscopy* **231**, 113254 (2021).

13. Good, P. F., Perl, D. P., Bierer, L. M. & Schmeidler, J. Selective accumulation of aluminum and iron in the neurofibrillary tangles of Alzheimer's disease: a laser microprobe (LAMMA) study. *Ann Neurol* **31**, 286–292 (1992).

14. SUNDBERG, R. D. & BROMAN, H. The Application of the Prussian Blue Stain to Previously Stained Films of Blood and Bone Marrow. *Blood* **10**, 160–166 (1955).

15. Schauenstein, E., Esterbauer, H., Jaag, G. & Taufer, M. Über die Wirkungen von Aldehyden auf gesunde und maligne Zellen, 1. Mitt.: Hydroxy-octenal, ein neuer Fettaldehyd. *Monatshefte für Chemie* **95**, 180–183 (1964).

16. Lovell, M. A., Ehmann, W. D., Mattson, M. P. & Markesbery, W. R. Elevated 4-hydroxynonenal in ventricular fluid in Alzheimer's disease. *Neurobiol Aging* **18**, 457–461 (1997).
17. Markesbery, W. R. & Lovell, M. A. Four-hydroxynonenal, a product of lipid peroxidation, is increased in the brain in Alzheimer's disease. *Neurobiol Aging* **19**, 33–36 (1998).
18. Sonowal, H. & Ramana, K. V. 4-Hydroxy-Trans-2-Nonenal in the Regulation of Anti-Oxidative and Pro-Inflammatory Signaling Pathways. *Oxid Med Cell Longev* **2019**, 5937326 (2019).
19. Kruman, I., Bruce-Keller, A. J., Bredesen, D., Waeg, G. & Mattson, M. P. Evidence that 4-hydroxynonenal mediates oxidative stress-induced neuronal apoptosis. *J Neurosci* **17**, 5089–5100 (1997).
20. Wang, F. *et al.* Iron Dyshomeostasis and Ferroptosis: A New Alzheimer's Disease Hypothesis? *Front Aging Neurosci* **14**, 830569 (2022).
21. Jakaria, M., Belaidi, A. A., Bush, A. I. & Ayton, S. Ferroptosis as a mechanism of neurodegeneration in Alzheimer's disease. *J Neurochem* **159**, 804–825 (2021).
22. Dharmalingam, P. *et al.* Pervasive Genomic Damage in Experimental Intracerebral Hemorrhage: Therapeutic Potential of a Mechanistic-Based Carbon Nanoparticle. *ACS Nano* **14**, 2827–2846 (2020).
23. Ayton, S., Faux, N. G., Bush, A. I., & Alzheimer's Disease Neuroimaging Initiative. Ferritin levels in the cerebrospinal fluid predict Alzheimer's disease outcomes and are regulated by APOE. *Nat Commun* **6**, 6760 (2015).
24. Ashraf, A., Jeandriens, J., Parkes, H. G. & So, P.-W. Iron dyshomeostasis, lipid peroxidation and perturbed expression of cystine/glutamate antiporter in Alzheimer's disease: Evidence of ferroptosis. *Redox Biol* **32**, 101494 (2020).
25. Grundke-Iqbal, I. *et al.* Ferritin is a component of the neuritic (senile) plaque in Alzheimer dementia. *Acta Neuropathol* **81**, 105–110 (1990).

26. Quintana, C. *et al.* Study of the localization of iron, ferritin, and hemosiderin in Alzheimer's disease hippocampus by analytical microscopy at the subcellular level. *J Struct Biol* **153**, 42–54 (2006).

27. Kenkhuis, B. *et al.* Iron loading is a prominent feature of activated microglia in Alzheimer's disease patients. *Acta Neuropathol Commun* **9**, 27 (2021).

28. Raha, A. A. *et al.* Interplay of Ferritin Accumulation and Ferroportin Loss in Ageing Brain: Implication for Protein Aggregation in Down Syndrome Dementia, Alzheimer's, and Parkinson's Diseases. *Int J Mol Sci* **23**, 1060 (2022).

29. Feng, H. & Stockwell, B. R. Unsolved mysteries: How does lipid peroxidation cause ferroptosis? *PLoS Biol* **16**, e2006203 (2018).

30. Hirschhorn, T. & Stockwell, B. R. The development of the concept of ferroptosis. *Free Radic Biol Med* **133**, 130–143 (2019).

31. Shih, A. Y. *et al.* Cystine/Glutamate Exchange Modulates Glutathione Supply for Neuroprotection from Oxidative Stress and Cell Proliferation. *J. Neurosci.* **26**, 10514–10523 (2006).

32. Chen, Y., Shertzer, H. G., Schneider, S. N., Nebert, D. W. & Dalton, T. P. Glutamate cysteine ligase catalysis: dependence on ATP and modifier subunit for regulation of tissue glutathione levels. *J Biol Chem* **280**, 33766–33774 (2005).

33. Wood, P. L. The Cerebellum in AD. in *Neuroinflammation: Mechanisms and Management* (ed. Wood, P. L.) 295–300 (Humana Press, 2003). doi:10.1007/978-1-59259-297-5_15.

34. Thorwald, M. A., Silva, J., Head, E. & Finch, C. E. Amyloid futures in the expanding pathology of brain aging and dementia. *Alzheimers Dement* (2022) doi:10.1002/alz.12896.

35. Stolwijk, J. M. *et al.* Red blood cells contain enzymatically active GPx4 whose abundance anticorrelates with hemolysis during blood bank storage. *Redox Biol* **46**, 102073 (2021).

36. Bryk, A. H. & Wiśniewski, J. R. Quantitative Analysis of Human Red Blood Cell Proteome. *J. Proteome Res.* **16**, 2752–2761 (2017).

37. LeVine, S. M., Wulser, M. J. & Lynch, S. G. Iron quantification in cerebrospinal fluid. *Anal Biochem* **265**, 74–78 (1998).

38. Erikson, K. M., Pinero, D. J., Connor, J. R. & Beard, J. L. Regional brain iron, ferritin and transferrin concentrations during iron deficiency and iron repletion in developing rats. *J Nutr* **127**, 2030–2038 (1997).

39. Petzold, A. *et al.* Cerebrospinal fluid ferritin levels, a sensitive diagnostic test in delayed presenting subarachnoid haemorrhage. *J Stroke Cerebrovasc Dis* **20**, 489–493 (2011).

40. Cazzola, M. *et al.* Biologic and clinical significance of red cell ferritin. *Blood* **62**, 1078–1087 (1983).

41. McIlwain, H. & Bachelard, H. S. *Biochemistry and the central nervous system*. (Churchill Livingstone, 1985).

42. Braak, H. & Braak, E. Neuropathological stageing of Alzheimer-related changes. *Acta Neuropathol* **82**, 239–259 (1991).

43. Xie, Z. *et al.* Peroxynitrite Mediates Neurotoxicity of Amyloid β-Peptide1–42- and Lipopolysaccharide-Activated Microglia. *J Neurosci* **22**, 3484–3492 (2002).

44. Dufrusine, B. *et al.* Iron-Dependent Trafficking of 5-Lipoxygenase and Impact on Human Macrophage Activation. *Front Immunol* **10**, 1347 (2019).

45. Montagne, A. *et al.* Blood-brain barrier breakdown in the aging human hippocampus. *Neuron* **85**, 296–302 (2015).

46. Bennett, D. A., Schneider, J. A., Bienias, J. L., Evans, D. A. & Wilson, R. S. Mild cognitive impairment is related to Alzheimer disease pathology and cerebral infarctions. *Neurology* **64**, 834–841 (2005).

47. Sundaresan, V. *et al.* Automated Detection of Candidate Subjects With Cerebral Microbleeds Using Machine Learning. *Front Neuroinform* **15**, 777828 (2021).

48. McCarter, S. J. *et al.* Association Between Plasma Biomarkers of Amyloid, Tau, and Neurodegeneration with Cerebral Microbleeds. *J Alzheimers Dis* **87**, 1537–1547 (2022).

49. Beaman, C. *et al.* Cerebral Microbleeds, Cerebral Amyloid Angiopathy, and Their Relationships to Quantitative Markers of Neurodegeneration. *Neurology* **98**, e1605–e1616 (2022).

50. Cacciottolo, M. *et al.* The APOE4 allele shows opposite sex bias in microbleeds and Alzheimer's disease of humans and mice. *Neurobiology of Aging* **37**, 47–57 (2016).

51. Nag, S. *et al.* Ex vivo MRI facilitates localization of cerebral microbleeds of different ages during neuropathology assessment. *Free Neuropathology* **2**, 35–35 (2021).

52. Cacciottolo, M., Morgan, T. E. & Finch, C. E. Age, sex, and cerebral microbleeds in EFAD Alzheimer disease mice. *Neurobiol Aging* **103**, 42–51 (2021).

53. Tai, L. M. *et al.* EFAD transgenic mice as a human APOE relevant preclinical model of Alzheimer's disease. *J Lipid Res* **58**, 1733–1755 (2017).

54. Arosio, P. & Levi, S. Ferritin, iron homeostasis, and oxidative damage1, 2 1Guest Editor: Mario Comporti 2This article is part of a series of reviews on "Iron and Cellular Redox Status." The full list of papers may be found on the homepage of the journal. *Free Radical Biology and Medicine* **33**, 457–463 (2002).

55. Collingwood, J. F. *et al.* Three-dimensional tomographic imaging and characterization of iron compounds within Alzheimer's plaque core material. *J Alzheimers Dis* **14**, 235–245 (2008).

56. van Duijn, S., Nabuurs, R. J. A., van Duinen, S. G. & Natté, R. Comparison of Histological Techniques to Visualize Iron in Paraffin-embedded Brain Tissue of Patients with Alzheimer's Disease. *J Histochem Cytochem* **61**, 785–792 (2013).

57. Streit, W. J. *et al.* Droplet Degeneration of Hippocampal and Cortical Neurons Signifies the Beginning of Neuritic Plaque Formation. *J Alzheimers Dis* **85**, 1701–1720 (2022).

58. Bush, A. I., Masters, C. L. & Tanzi, R. E. Copper, β-amyloid, and Alzheimer's disease: Tapping a sensitive connection. *Proceedings of the National Academy of Sciences* **100**, 11193–11194 (2003).

59. Rogers, J. T. *et al.* An iron-responsive element type II in the 5'-untranslated region of the Alzheimer's amyloid precursor protein transcript. *J Biol Chem* **277**, 45518–45528 (2002).

60. Bodovitz, S., Falduto, M. T., Frail, D. E. & Klein, W. L. Iron levels modulate alpha-secretase cleavage of amyloid precursor protein. *J Neurochem* **64**, 307–315 (1995).

61. Yamamoto, A. *et al.* Iron (III) induces aggregation of hyperphosphorylated tau and its reduction to iron (II) reverses the aggregation: implications in the formation of neurofibrillary tangles of Alzheimer's disease. *J Neurochem* **82**, 1137–1147 (2002).

62. Sadleir, K. R. *et al.* Presynaptic dystrophic neurites surrounding amyloid plaques are sites of microtubule disruption, BACE1 elevation, and increased Aβ generation in Alzheimer's disease. *Acta Neuropathol* **132**, 235–256 (2016).

63. Muñoz-Castro, C. *et al.* Cyclic multiplex fluorescent immunohistochemistry and machine learning reveal distinct states of astrocytes and microglia in normal aging and Alzheimer's disease. *J Neuroinflammation* **19**, 30 (2022).

64. Zeineh, M. M. *et al.* Activated iron-containing microglia in the human hippocampus identified by magnetic resonance imaging in Alzheimer disease. *Neurobiol Aging* **36**, 2483–2500 (2015).

65. Reinert, A., Morawski, M., Seeger, J., Arendt, T. & Reinert, T. Iron concentrations in neurons and glial cells with estimates on ferritin concentrations. *BMC Neuroscience* **20**, 25 (2019).

66. Arai, M. *et al.* Import into mitochondria of phospholipid hydroperoxide glutathione peroxidase requires a leader sequence. *Biochem Biophys Res Commun* **227**, 433–439 (1996).

67. Lu, B. *et al.* Identification of PRDX6 as a regulator of ferroptosis. *Acta Pharmacologica Sinica* **40**, 1334–1342 (2019).

68. Sun, J. *et al.* Identification of a Novel Ferroptosis-Related Gene Prognostic Signature in Bladder Cancer. *Front Oncol* **11**, 730716 (2021).

69. Chatterjee, S. *et al.* Peroxiredoxin 6 phosphorylation and subsequent phospholipase A2 activity are required for agonist-mediated activation of NADPH oxidase in mouse pulmonary microvascular endothelium and alveolar macrophages. *J Biol Chem* **286**, 11696–11706 (2011).

70. Vázquez-Medina, J. P. *et al.* Genetic inactivation of the phospholipase A2 activity of peroxiredoxin 6 in mice protects against LPS-induced acute lung injury. *Am J Physiol Lung Cell Mol Physiol* **316**, L656–L668 (2019).

71. Fisher, A. B. Peroxiredoxin 6 in the repair of peroxidized cell membranes and cell signaling. *Arch Biochem Biophys* **617**, 68–83 (2017).

72. Lubos, E., Loscalzo, J. & Handy, D. E. Glutathione Peroxidase-1 in Health and Disease: From Molecular Mechanisms to Therapeutic Opportunities. *Antioxid Redox Signal* **15**, 1957–1997 (2011).

73. Gwon, A.-R. *et al.* Oxidative lipid modification of nicastrin enhances amyloidogenic γ-secretase activity in Alzheimer's disease. *Aging Cell* **11**, 559–568 (2012).

74. Kwak, Y.-D. *et al.* Differential regulation of BACE1 expression by oxidative and nitrosative signals. *Molecular Neurodegeneration* **6**, 17 (2011).

75. Fukumoto, H., Cheung, B. S., Hyman, B. T. & Irizarry, M. C. Beta-secretase protein and activity are increased in the neocortex in Alzheimer disease. *Arch Neurol* **59**, 1381–1389 (2002).

76. Zhong, H. & Yin, H. Role of lipid peroxidation derived 4-hydroxynonenal (4-HNE) in cancer: Focusing on mitochondria. *Redox Biology* **4**, 193–199 (2015).

77. Zuliani, G. *et al.* Increased blood BACE1 activity as a potential common pathogenic factor of vascular dementia and late onset Alzheimer's disease. *Sci Rep* **10**, 14980 (2020).

78. Hampel, H. *et al.* The β-Secretase BACE1 in Alzheimer's Disease. *Biological Psychiatry* **89**, 745–756 (2021).

79. McGrath, L. T. *et al.* Increased oxidative stress in Alzheimer's disease as assessed with 4-hydroxynonenal but not malondialdehyde. *QJM* **94**, 485–490 (2001).

80. Smith, M. A., Harris, P. L. R., Sayre, L. M. & Perry, G. Iron accumulation in Alzheimer disease is a source of redox-generated free radicals. *Proceedings of the National Academy of Sciences* **94**, 9866–9868 (1997).

81. M, R.-G. *et al.* Sensitivity to carcinogenesis is increased and chemoprotective efficacy of enzyme inducers is lost in nrf2 transcription factor-deficient mice. *Proceedings of the National Academy of Sciences of the United States of America* **98**, (2001).

82. Aa, S. *et al.* Regulation of selenoprotein GPx4 expression and activity in human endothelial cells by fatty acids, cytokines and antioxidants. *Atherosclerosis* **171**, (2003).

83. Zhang, H. *et al.* Nrf2-regulated phase II enzymes are induced by chronic ambient nanoparticle exposure in young mice with age-related impairments. *Free Radic. Biol. Med.* **52**, 2038–2046 (2012).

84. Zhou, L., Zhang, H., Davies, K. J. A. & Forman, H. J. Aging-related decline in the induction of Nrf2-regulated antioxidant genes in human bronchial epithelial cells. *Redox Biol* **14**, 35–40 (2018).

85. Wardyn, J. D., Ponsford, A. H. & Sanderson, C. M. Dissecting molecular cross-talk between Nrf2 and NF-κB response pathways. *Biochem Soc Trans* **43**, 621–626 (2015).

86. Gao, W. *et al.* Dissecting the Crosstalk Between Nrf2 and NF-κB Response Pathways in Drug-Induced Toxicity. *Front Cell Dev Biol* **9**, 809952 (2021).

87. Provasek, V. E., Mitra, J., Malojirao, V. H. & Hegde, M. L. DNA Double-Strand Breaks as Pathogenic Lesions in Neurological Disorders. *Int J Mol Sci* **23**, 4653 (2022).

88. Shanbhag, N. M. *et al.* Early neuronal accumulation of DNA double strand breaks in Alzheimer's disease. *Acta Neuropathol Commun* **7**, 77 (2019).

89. Miller, M. B., Reed, H. C. & Walsh, C. A. Brain Somatic Mutation in Aging and Alzheimer's Disease. *Annu Rev Genomics Hum Genet* **22**, 239–256 (2021).

90. Crapper McLachlan, D. R. *et al.* Intramuscular desferrioxamine in patients with Alzheimer's disease. *Lancet* **337**, 1304–1308 (1991).

91. Gleason, A. & Bush, A. I. Iron and Ferroptosis as Therapeutic Targets in Alzheimer's Disease. *Neurotherapeutics* **18**, 252–264 (2021).

92. Keberle, H. THE BIOCHEMISTRY OF DESFERRIOXAMINE AND ITS RELATION TO IRON METABOLISM. *Ann N Y Acad Sci* **119**, 758–768 (1964).

93. Li, Q. *et al.* Neuroprotection of brain-permeable iron chelator VK-28 against intracerebral hemorrhage in mice. *J Cereb Blood Flow Metab* **37**, 3110–3123 (2017).

94. Shachar, D. B., Kahana, N., Kampel, V., Warshawsky, A. & Youdim, M. B. H. Neuroprotection by a novel brain permeable iron chelator, VK-28, against 6-hydroxydopamine lession in rats. *Neuropharmacology* **46**, 254–263 (2004).

95. Graham, U. M. *et al.* Tissue Specific Fate of Nanomaterials by Advanced Analytical Imaging Techniques - A Review. *Chem Res Toxicol* **33**, 1145–1162 (2020).

96. Cacciottolo, M. *et al.* OXIDATIVE STRESS FROM TRAFFIC-RELATED AIR POLLUTANTS (TRAP) INDUCES PRO-AMYLOIDOGENIC LIPID RAFT ALTERATION IN AD MODELS. *Alzheimer's & Dementia: The Journal of the Alzheimer's Association* **14**, P1124–P1125 (2018).

97. Cheng, H. *et al.* Nanoscale Particulate Matter from Urban Traffic Rapidly Induces Oxidative Stress and Inflammation in Olfactory Epithelium with Concomitant Effects on Brain. *Environ Health Perspect* **124**, 1537–1546 (2016).

98. Kayed, R. *et al.* Fibril specific, conformation dependent antibodies recognize a generic epitope common to amyloid fibrils and fibrillar oligomers that is absent in prefibrillar oligomers. *Mol Neurodegeneration* **2**, 18 (2007).

99. Thorwald, M. *et al.* Angiotensin receptor blockade improves cardiac mitochondrial activity in response to an acute glucose load in obese insulin resistant rats. *Redox Biol* **14**, 371–378 (2018).

100. Thorwald, M. A. *et al.* Nrf2-related gene expression is impaired during a glucose challenge in type II diabetic rat hearts. *Free Radic. Biol. Med.* **130**, 306–317 (2019).

101. Dimauro, I., Pearson, T., Caporossi, D. & Jackson, M. J. A simple protocol for the subcellular fractionation of skeletal muscle cells and tissue. *BMC Res Notes* **5**, 513 (2012).